CAAP Annual Report

Date of Report: *09/30/2024*

Prepared for: *U.S. DOT Pipeline and Hazardous Materials Safety Administration*

Annual Period: **From** *(October 1, 2023)* **to** *(September 30, 2024)*

Contract Number: *693JK32350004CAAP*

Project Title: *Multi-Compound Green Corrosion Inhibitor for Gas Pipeline: Synthesis, Optimization, and Evaluation*

Prepared by: *Dr. Yongming Liu (PI), Dr. Shuguang Deng (Co-PI), Dr. Tekle Fida (Co-PI), Xuandong Lu, Saumya Mehta, Mohammadjavad Kazemi, Sai Niranjan*

Contact Info.: *480-965-6883*

yongming.liu@asu.edu

Table of Contents

Section A: Business and Activities

Contract Activities

Contract Modifications:

Educational Activities:

- Student mentoring: Sai Niranjan (M.S.), Mohammadjavad Kazemi (Ph.D.), Essam Abdel Rahman (visiting scholar), Qihang Xu (Ph.D.), Saumya Dimple Mehta (M.S.), Xuandong Lu (Ph.D.), Kapil Chandra Akula (M.S.)
- Student internship:
- Educational activities: Sponsored a FURI student (Emma Estrada)
- Career employed: None
- Others: None

Dissemination of Project Outcomes: None

Citations of The Publications: None

Others: None

Financial Summary

- A separate financial report will be submitted by ASU financial office.

Project Schedule Update

Project Schedule: On schedule

Corrective Actions: None

Status Update of the 4th or 8th Quarter Technical Activities

Task 1.2: Synthesis and Characterization of Green Inhibitors from Renewable Feedstock

1) *Developed techniques to chemically modify pectin, improving its corrosion resistance by cross-linking and optimizing its adhesion properties for better performance in harsh environments.*

2) *Enhanced pectin's inhibition efficiency by increasing its adsorption on metal*

surfaces, achieved through the incorporation of additional active functional groups using EDC (1-Ethyl-3-(3-dimethyl aminopropyl) carbodiimide) and NHS (N-Hydroxysuccinimide).

Task 1.3: Corrosion Testing for Verification and Validation

1) *Compare the corrosion behavior of A36 and API 5L steel coupons, addressing concerns about the suitability of A36 for corrosion tests typically performed with API 5L steel used in gas pipelines.*

2) *Established a performance baseline using industry-standard chemical inhibitors to benchmark and compare the effectiveness of green inhibitors.*

3) *Designed and implemented a turbulent flow corrosion testing system to replicate real-world pipeline conditions, improving the assessment of inhibitors under dynamic flow conditions.*

Task 2.1: Numerical simulation of multiphase flow for inhibitor distribution in gas pipeline systems

1) *Employed CFD methods to model the dynamics of multiphase flow within gas pipelines.*

Task 2.2: AI-assisted inhibitor implementation optimization in gathering and transportation pipelines

1) *Established the prediction framework for wall shear stress with uncertainty quantification.*

2) *Applied the dimensionality reduction approach in predicting the temporal development of partial differential equations.*

3) *Established the multi-fidelity framework for the efficient prediction of flow parameters.*

Section B: Detailed Technical Results in the Report Period

1. Background and Objectives in the 1st Annual Report Period

Background

Corrosion in pipelines poses a significant threat to the integrity, safety, and efficiency of fluid and gas transportation systems. Addressing this issue has become increasingly urgent as industries seek environmentally sustainable and effective solutions. In recent years, the development of green inhibitors—derived from renewable sources—has emerged as a promising approach, aligning with the global push toward sustainable industrial practices. Green inhibitors offer an eco-friendly alternative to conventional, petroleum-based inhibitors, which have long been associated with environmental harm and concerns about resource depletion.

Traditionally, corrosion inhibitors were synthesized from petroleum-based compounds, many of which are toxic, non-biodegradable, and reliant on non-renewable resources. This has raised the alarm regarding their long-term environmental impact, spurring researchers to explore green inhibitors derived from natural, renewable materials such as agricultural by-products, plant extracts, and waste biomass. These bio-based inhibitors not only mitigate corrosion but also contribute to waste reduction and resource sustainability.

The synthesis of green inhibitors involves a systematic, multi-faceted process. It begins with a comprehensive literature review to identify candidates with potential corrosion-inhibiting properties. This review encompasses a broad spectrum of organic compounds, including plant-based polyphenols, flavonoids, and alkaloids, known for their ability to form protective films on metal surfaces. Additionally, close collaboration with industry advisory boards ensures that the green inhibitors under development meet existing industry standards for safety, efficiency, and compatibility with current pipeline materials and transported fluids.

A critical stage in this process is converting renewable feedstock into effective corrosion inhibitors. For example, natural resources like citrus peels have been studied for their ability to be transformed into pectin, a polysaccharide with promising corrosion-resistant properties. This transformation involves the development of experimental protocols that ensure both the reproducibility of the synthesis process and its scalability for industrial application.

In the context of pipeline corrosion protection, green inhibitors offer dual benefits: not only do they inhibit corrosion, but they also advance sustainable practices by utilizing otherwise discarded

waste materials. One notable case is the conversion of citrus peel waste into pectin, which has demonstrated strong potential as a corrosion inhibitor. These inhibitors, derived from natural products, help minimize the environmental footprint of pipeline operations while maintaining or even improving corrosion resistance.

In Task 1, our investigative efforts have been guided by an exhaustive literature review, which has illuminated various pathways toward identifying effective green corrosion inhibitors. This foundational work has been further supported by the development of specialized experimental protocols designed to optimize the conversion of renewable feedstocks into potent corrosion mitigation agents. Additionally, by consulting industry standards and engaging with industrial partners, we have ensured that the inhibitors we develop are both compatible with existing pipeline materials and aligned with operational safety requirements.

The successful synthesis of pectin from orange peels is a milestone in our project, marking the first step toward establishing a robust framework for comprehensive corrosion testing methodologies. This has set the stage for more advanced phases of research, which will focus on refining these inhibitors and testing them under real-world pipeline conditions. As our research progresses, we emphasize the detailed characterization of the synthesized inhibitors, including their chemical composition, molecular structure, and corrosion-inhibiting mechanisms. This involves employing advanced analytical techniques such as electrochemical impedance spectroscopy (EIS), scanning electron microscopy (SEM), and Fourier-transform infrared spectroscopy (FTIR) to validate the performance of the green inhibitors in simulated corrosion environments. This characterization is crucial for understanding how these bio-derived inhibitors function and for optimizing their efficacy in protecting pipeline infrastructure.

In Task 2, we aim at AI-enhanced simulation for the temporal development of inhibitor particles after their injection in the pipe system. We mainly consider flow-induced degradation primarily attributed to the fluid dynamics within the pipeline, where multiple phases of matter - gases and occasionally solid inhibitor particles - interact with the inner walls. Compared to the static state, this interaction more likely to trigger the disintegration of the protective inhibitor layer, leaving the metal surface vulnerable to corrosive agents, in which wall shear stress (WSS) serves as a key metric for assessing the impact of multiphase flow on corrosion inhibitor films. At this point, we innovatively proposed a surrogate model on the microscopic level to predict WSS with different spatial roughness profile and further incorporated uncertainty quantification.

Microscale studies cannot take into account the global flow field and are required to configure appropriate boundary conditions. As the latest progress, we conducted a macroscopic analysis of the artificially enhanced flow field, laying the foundation for boundary determination and further study of injection and transportation characteristics of corrosion inhibitors. Specifically, we focus on two types of approaches for the efficiency of obtaining desired flow data when ensuring accuracy: 1) multi-fidelity approach and 2) partial differential equation (PDE) solution with dimensionality reduction. The former contains a Bayesian convolutional neural network with adaptive sampling that produces high-fidelity data from low-fidelity data. The latter builds a physics-informed temporal prediction model based on a pre-trained autoencoder, which serves to reduce the original flow filed into the latent space for more efficient prediction. We performed many comparison studies in the above models, which are crucial for our understanding of parameter configurations in different cases.

Through these efforts, we aim to contribute to the growing field of sustainable corrosion protection, advancing both the science of green inhibitors and their practical application in industries where pipeline corrosion remains a critical challenge.

Objectives in the 1st Annual Report Period

The primary objectives of Task 1 in the first year are two-fold: first, to conduct an extensive literature survey to identify potential candidates for green corrosion inhibitors, focusing on renewable feedstocks such as plant extracts, bio-based wastes, and microbial enzymes. This will inform the establishment of synthesis protocols for extracting active constituents from these sustainable resources. Second, we aim to develop and standardize testing methods for the verification and validation of these green inhibitors. An additional goal of this task is to consult with our industry advisory board to ensure that our inhibitors meet current industry standards for compatibility and safety, thus aligning our work with practical and real-world applications.

For Task 2, we focus on performing CFD to simulate inhibitor injection to optimize key parameters including injection locations, injection rate, inhibitor concentration, inhibitor density and particle size. Corresponding AI-enhanced approach is simultaneously improved for a more efficient prediction under various flow scenarios. Besides, the research seeks to understand inhibitor degradation under flow conditions, which is based on the prediction model of WSS and circulation experiment of corrosion rate in Task 1.

During the project kickoff meeting, Dr. Zhongquan Zhou, addressed the MRP reviewer panel's feedback on our proposal. She emphasized the importance of expanding our research scope to include a thorough investigation into these comments, particularly regarding the subject of corrosion protection using bio-based materials.

In parallel with the synthesis and optimization efforts, the project is equally dedicated to the rigorous development and refinement of corrosion testing methodologies. We are establishing comprehensive protocols, including both weight-loss and electrochemical measurements, to evaluate the corrosion inhibition efficacy of the bio-derived inhibitors. This integrated approach ensures that the innovation in green inhibitor development is supported by reliable, reproducible testing methods, creating a robust framework for accurate assessment.

By balancing cutting-edge synthesis with methodical validation, our multidisciplinary project is poised to make significant contributions to the field of sustainable corrosion protection. Ultimately, we aim to address critical industrial needs for safety, efficiency, and environmental stewardship through the development of bio-based corrosion inhibitors.

2. Experimental Program in the 1st Annual Report Period

2.1 Experimental Design

2.1.1 Extraction of pectin from citrus peels

We explored several methods for converting citrus peel into pectin and optimizing its use as a green inhibitor for gas pipeline corrosion protection. The extraction of pectin from citrus peel is a delicate and critical process that requires precision to ensure high-quality pectin with the desired properties for corrosion inhibition. Various extraction techniques have been employed, each offering distinct advantages and challenges. Below is a comparison of the most commonly used methods for extracting pectin from citrus peel:

Table 1.1. Summary of Experimental Methods for Extracting Pectin from Citrus Peels

Method	Method Description	Pros	Cons
Conventional Acid Extraction	The citrus peel is subjected to acid hydrolysis using mineral acids such as hydrochloric acid or sulfuric acid.	This method is relatively straightforward and has been widely used in the industry for its efficiency.	It may result in a lower yield of pectin due to the potential degradation of pectin molecules during prolonged exposure to high temperatures and acidic conditions.
Enzyme-Assisted Extraction	Enzymes, particularly pectinase, are employed to break down the cell wall structures, facilitating the release of pectin.	This method is considered gentler, preserving the structural integrity of pectin and potentially yielding pectin with better functional properties.	Enzyme extraction may be time-consuming and might require optimization of enzyme concentrations and incubation periods.
Microwave-Assisted Extraction	The application of microwave energy accelerates the extraction process by promoting the breakdown of cell walls.	It is known for its rapid extraction, reduced solvent usage, and potential preservation of pectin structure.	Optimization of microwave parameters is crucial, and there may be concerns about the potential degradation of pectin under certain conditions.
Ultrasound-Assisted Extraction	Ultrasonic waves aid in the disruption of cell walls, facilitating the release of pectin.	It is recognized for its efficiency, reduced extraction time, and potential to yield pectin with improved physicochemical properties.	Optimal conditions, including frequency and amplitude, need to be carefully adjusted to avoid potential degradation.
Combined Methods	Some studies combine different extraction techniques, such as enzyme-assisted extraction followed by conventional acid extraction, to leverage the advantages of each method.	Combining methods can enhance extraction efficiency and pectin yield while mitigating the drawbacks of individual techniques.	The process complexity and increased resource requirements may be considerations.

In conclusion, the choice of extraction method for pectin from citrus peel depends on factors such as desired pectin properties, efficiency, and scalability. Researchers often explore multiple

methods to optimize conditions and enhance the overall extraction process, ensuring the production of high-quality pectin for various industrial applications.

We have conducted a detailed study to refine the extraction and synthesis process of pectin from orange peels. Pectin, a naturally occurring polysaccharide predominantly found in the cell walls of terrestrial plants, particularly within the rinds of fruits, stands as a testament to the sophistication of nature's design. This biopolymer is primarily composed of repeating units of galacturonic acid, which coalesce to form a flexible and intricately branched polymer structure. The presence of carboxyl (-COOH) and hydroxyl (-OH) functional groups within its structure endows pectin with its characteristic water solubility and unique ability to form gels under certain conditions.

The application of pectin as a green corrosion inhibitor represents a paradigm shift towards more environmentally sustainable practices in metal protection. The traditional approach to corrosion inhibition, often reliant on synthetic chemicals, faces increasing scrutiny due to environmental and health concerns. Pectin, with its biodegradable nature and low toxicity, emerges as an eco-friendly alternative, aligning with the growing demand for sustainable industrial solutions.

When applied to steel surfaces, pectin leverages its carboxyl and hydroxyl groups to form a protective barrier against corrosive agents. This barrier is believed to adhere to the metal surface, thus inhibiting the electrochemical processes that lead to corrosion. The efficacy of pectin in this role is attributed to its ability to form stable complexes with metal ions, a property that significantly reduces the metal's susceptibility to oxidative reactions that cause rusting. Furthermore, the gel-forming capability of pectin could play a crucial role in sealing the metal surface from corrosive environments, thereby extending the lifespan of steel structures without the adverse environmental impacts associated with conventional corrosion inhibitors.

This growing field of research into the application of pectin as a corrosion inhibitor for steel and other metals holds promise not only for the protection of critical infrastructure but also for the advancement of green chemistry and sustainable materials science. As the scientific community continues to explore and understand the mechanisms behind pectin's inhibitory effects, the potential for broader application and the development of more effective, eco-friendly corrosion prevention strategies becomes increasingly apparent.

Building on our initial literature review on the extraction of pectin from orange peels, we extensively attempt to optimize the process of extraction and synthesis of pectin.

The extraction of pectin from citrus peels involves a series of methodical procedures aimed at isolating this valuable polysaccharide with precision and efficiency. The process utilizes a combination of chemical and physical methods to ensure the breakdown of cell walls and the subsequent release of pectin. Herein, we detail the step-by-step approach adopted in our experiment.

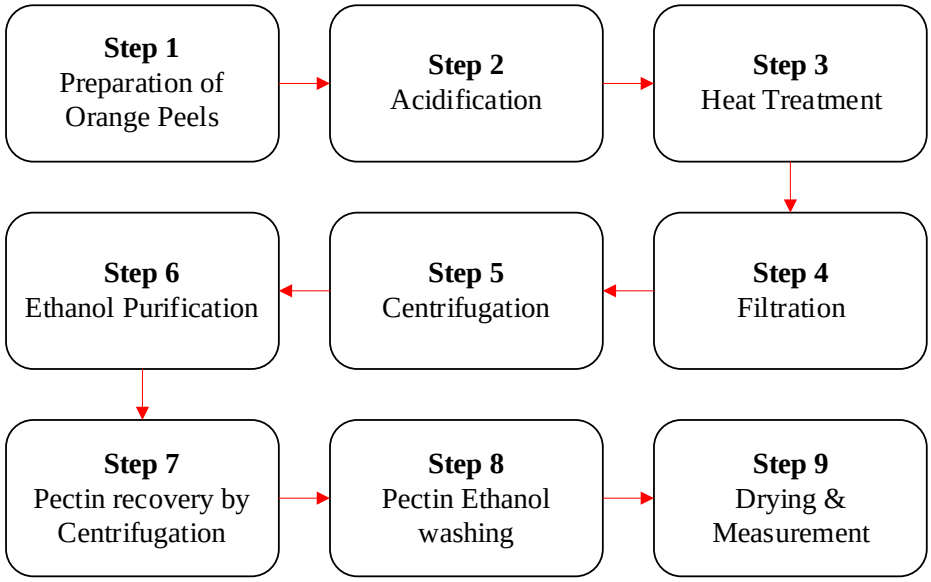

Figure 1.1. Basic steps for pectin extraction from citrus peels

Step 1. Preparation of Orange Peels:

- The orange peels were initially subjected to cutting to enhance the surface area available for extraction.
- Subsequent washing was performed to remove any adhering dirt or contaminants.
- Post-washing, the peels were thoroughly dried to eliminate excess moisture.

Step 2. Measurement and Acidification:

- A precise weight of 45 grams of the prepared orange peel was measured to ensure consistency.
- These were then placed into a container with 500 ml of deionized water.
- Hydrochloric acid (HCl) was added dropwise to the solution to achieve a pH level of 1.0, facilitating the disruption of pectin-containing cell walls within the peels.

Step 3. Heat Treatment:

- The acidified mixture was transferred to a beaker and subjected to heat treatment.
- A constant temperature of 90°C was maintained for 3 hours, with continuous stirring to promote uniform heating and prevent charring.

Step 4. Filtration:

- After heating, the hot solution was filtered to remove the solid remnants of the orange peels.
- The filtration utilized a fine-mesh material capable of allowing the passage of the pectin-rich solution while retaining the bulky solids.

Step 5. Centrifugation:

- The filtered solution was subjected to centrifugation at a speed of 4000 rpm for 15 minutes.
- This process aided in the separation of the pectin from other soluble impurities.

Step 6. Ethanol Purification:

- Post-centrifugation, the pectin was precipitated by adding 98% Ethanol.
- The addition of ethanol precipitated the pectin, enabling its separation from the aqueous phase.

Step 7. Centrifugation:

- The Ethanol precipitated solution was subjected to another centrifugation at a speed of 4000 rpm for 15 minutes.

Step 8. Pectin Washing:

- Post-centrifugation, the pectin was washed with 60% Ethanol.

Step 9. Drying:

- The precipitated pectin was carefully collected and spread evenly on a drying tray.
- This was placed in an oven preheated to 60°C for 4 hours, ensuring thorough drying without degradation.
- The dried pectin was weighed to quantify the yield.

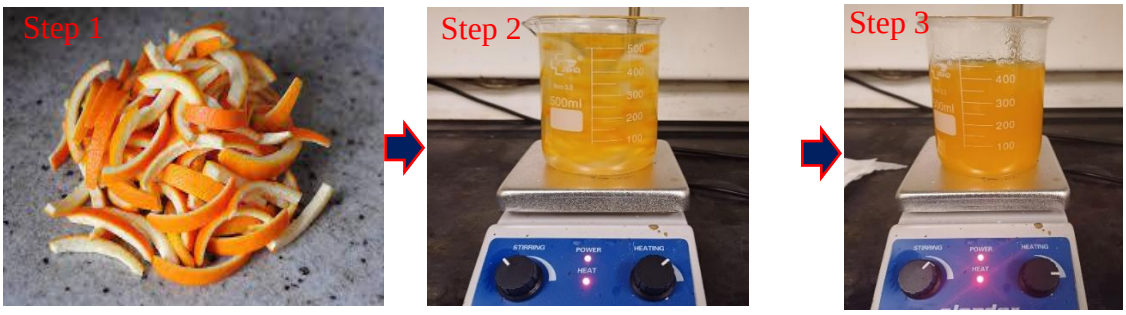

Figure 1.2. Illustration of the conducted pectin extraction process

Figure 1.2 is an illustration of the conducted extraction process. Throughout this methodology, careful attention was paid to maintaining the integrity of the pectin structure. The process aimed at maximizing the yield.

2.1.2 Modification of pectin derived from citrus peels

We have developed advanced techniques to chemically modify pectin, enhancing its corrosion resistance through cross-linking and improving its adhesion properties for better performance in harsh environments. As part of Task 1.2, our primary focus was on establishing a method to boost pectin's corrosion inhibition efficiency via a series of strategic chemical modifications. These modifications were designed to augment pectin’s protective capabilities by employing cross-linking techniques and optimizing its adhesion to surfaces, thus improving its overall effectiveness under severe environmental conditions.

To begin, we dissolved 10 grams of pectin in 300 mL of deionized water. To this solution, we added 50 mmol of EDC (1-Ethyl-3-(3-dimethylaminopropyl) carbodiimide) and 16.7 mmol of NHS (N-Hydroxysuccinimide). This mixture was stirred continuously in an ice bath for three hours. This activation step was crucial, as it rendered the carboxyl groups of the pectin more reactive, thereby preparing the polymer for subsequent chemical modifications.

Following the activation phase, we dissolved 50 mmol of an amino acid in an additional 300 mL of deionized water, which was then mixed with the activated pectin solution. The pH of this combined solution was carefully adjusted to 5 using a 1 mol/L hydrochloric acid solution, creating optimal conditions for the grafting reaction.

To initiate the grafting reaction, the mixture was magnetically stirred for 24 hours under the same ice bath conditions. This extended stirring period was essential to ensure a complete reaction

and successful formation of the modified pectin, which exhibited enhanced adhesive properties and improved molecular stability.

After the reaction, 600 mL of anhydrous ethanol was added to the mixture to precipitate the modified pectin. The precipitate was then collected through centrifugation, followed by thorough dialysis against a 7000–14000 Dalton molecular weight cut-off membrane for 72 hours at room temperature. This dialysis process was critical for removing any unreacted EDC, amino acids, and NHS, ensuring the purity of the final product.

Finally, the purified pectin was freeze-dried, yielding a powder form of the chemically modified pectin. This refined biopolymer, enriched with new functional groups and a strengthened molecular structure, exhibits significantly improved corrosion-inhibitive properties, making it a promising candidate for use in protective coatings in aggressive environments.

We sought to enhance pectin's corrosion inhibition efficiency by increasing its adsorption onto metal surfaces. This was achieved by incorporating additional active functional groups using EDC (1-Ethyl-3-(3-dimethylaminopropyl)carbodiimide) and NHS (N-Hydroxysuccinimide) as coupling agents. Following this established method, pectin was successfully modified. Figure 1.3 illustrates the modification process and the resulting product. The modified pectin has since been tested for its effectiveness in corrosion inhibition, demonstrating promising results.

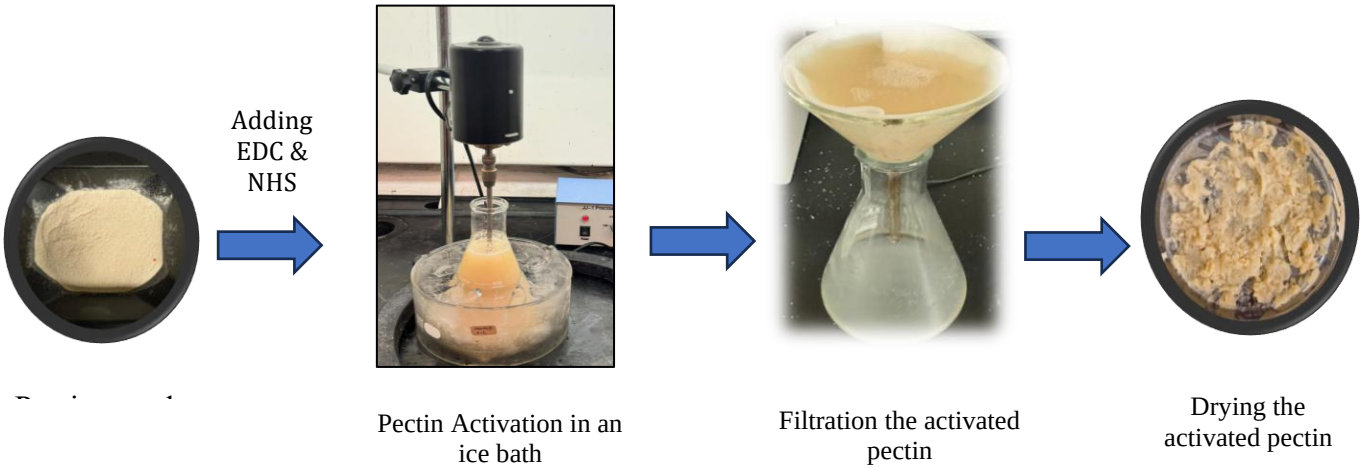

Figure 1.3. The conducted process for activation of pectin

In the process of modifying pectin using EDC and NHS, the activation and subsequent coupling of carboxyl groups enhance the pectin's functional properties, particularly its viscosity. This modification typically involves the introduction of amine groups via amide bond formation,

which leads to a change in the molecular structure of pectin. The newly introduced covalent bonds and possibly the formation of a network-like structure increase the overall molecular weight and cross-link density of the pectin.

This structural modification impacts the rheological properties of the pectin, most notably its viscosity. The cross-linked pectin exhibits higher viscosity compared to its unmodified counterpart due to the formation of a more tangled or structured polymer network. This network restricts the flow of the polymer chains relative to each other, thus increasing the resistance to deformation or flow. As a gel, the modified pectin is not just thicker but also more stable.

2.1.3 Preliminary experiments on extraction and synthesis of chitin and chitosan from shrimp shells

We have initiated preliminary research on extracting and synthesizing chitin and chitosan from shrimp shells, identifying them as promising green corrosion inhibitors. A detailed protocol was developed and followed for extracting chitosan. Shrimp shells were sourced from a local fish market and purified to ensure the removal of impurities. High-purity chemical reagents were used throughout the process to maintain the integrity and quality of the extraction. The extraction methodology involved a systematic approach, including deproteinization, demineralization, and deacetylation steps, which effectively yielded high-quality chitosan from the shrimp shells.

Step 1: Preparation of Shrimp Shell Powder

Initially, the shrimp shells were cleansed and then dried in an oven at 65 ℃ for 4 days until completely dehydrated. The dried shells were subsequently ground into a fine powder, which was stored in a sealed container and preserved in a freezer to maintain the shell's properties.

Step 2: Deproteinization

For deproteinization, 15 g of the shrimp shell powder underwent alkaline treatment, being mixed with 75 ml of 1 M sodium hydroxide solution (a 1:5 w/v ratio). This mixture was then heated and stirred at 30℃ for 20 hours. Following the alkaline treatment, the mixture was filtered and thoroughly washed with distilled water until a neutral pH of 7 was attained. After reaching a neutral pH, the powder was oven-dried overnight at 60 ℃, preparing it for the subsequent demineralization step.

Step 3: Demineralization

In the demineralization phase, the deproteinized shrimp shell powder was treated with a 2% hydrochloric acid solution, maintaining a solid-to-solvent ratio of 1:5 (w/v). The mixture was

stirred continuously at 30℃ for 16 hours. Post-treatment, the residue was filtered and again washed with distilled water until the pH returned to neutral. The resulting material was dried overnight in an oven, yielding chitin.

Step 4: Deacetylation

The deacetylation process involved treating chitin with a strong 50% (w/v) sodium hydroxide solution to remove the acetyl groups, thus converting chitin into chitosan. This reaction was conducted at 60 ℃, with a solid-to-solvent ratio of 1:10 (w/v) for 20 hours. Following the deacetylation, the material was washed with water until a neutral pH was achieved and then dried in an oven for 15 hours at 60 ℃ to obtain chitosan. Figure 1.4 illustrates the conducted procedure for the extraction of chitosan from Shrimp shells

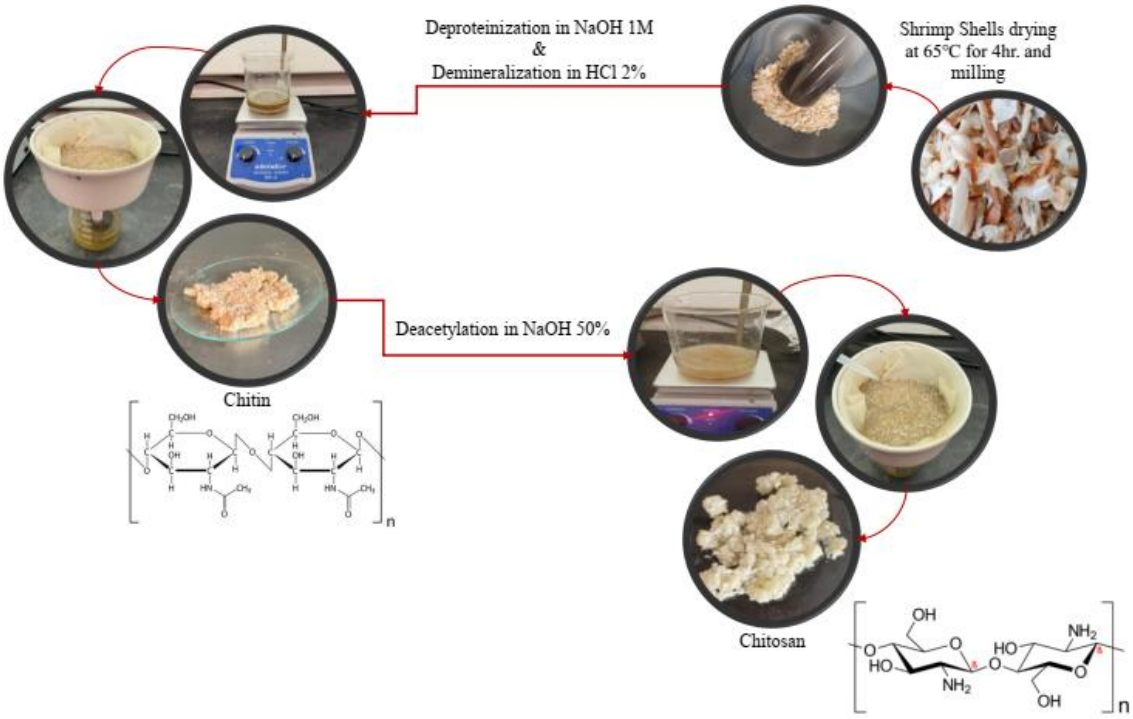

Figure 1.4. Chitosan extraction process from shrimp shells

In summary, during this reporting period, our team achieved significant progress in the design and synthesis of green corrosion inhibitors. Key accomplishments include the successful optimization of pectin extraction from orange peels, the initial synthesis of chitosan from shrimp shells, and the development of rigorous corrosion testing protocols. These efforts have laid a solid foundation for future work, including further functionalization of pectin, refinement of chitosan-

derived inhibitors, and comprehensive evaluation of their corrosion inhibition capabilities.

2.2 Test Procedure

Laboratory Testing:

We have completed an extensive review of corrosion testing methodologies and are continuing to develop and refine testing protocols. Evaluating green inhibitors has become crucial in advancing sustainable corrosion mitigation strategies. A range of techniques is employed to assess the effectiveness of these eco-friendly inhibitors in protecting gas pipelines from corrosion. The table below provides a comparative overview of the key test methods used to evaluate the performance of green inhibitors.

Table 1.2. Summary of Analytical Methods for Evaluating Green Inhibitors

Method	Method Overview	Advantages	Considerations
Electrochemical Methods	Potentiodynamic polarization, electrochemical impedance spectroscopy, and linear polarization resistance are commonly employed for their sensitivity in detecting changes at the metal interface.	Electrochemical methods provide real-time data, allowing for the quantitative assessment of corrosion parameters, including polarization resistance and corrosion current density.	Proper interpretation of electrochemical data requires a comprehensive understanding of the inhibitor's impact on the corrosion kinetics.
Weight Loss Measurements	Weight loss tests involve exposing metal specimens to corrosive environments with and without inhibitors and measuring the mass loss over time.	It offers a straightforward and cost-effective means of quantifying corrosion rates.	Environmental factors and variability in specimen geometry may influence the accuracy of weight loss measurements.
SEM and XRD	SEM and XRD are utilized for morphological and structural analyses of corroded surfaces, providing insights into the protective mechanisms of green inhibitors.	These techniques offer valuable information on the nature of corrosion products and inhibitor film formation.	SEM and XRD are often employed in conjunction with other quantitative methods for a comprehensive corrosion assessment.
Salt Spray Testing	Salt spray tests simulate aggressive corrosive environments to evaluate the protective efficacy of green inhibitors.	These tests provide accelerated corrosion conditions, allowing for the rapid assessment of inhibitor performance.	The correlation between accelerated testing and real-world performance should be carefully considered.
Microbiologically Influenced Corrosion (MIC) Testing	MIC tests assess the ability of green inhibitors to mitigate corrosion induced by microbial activity.	Relevant for applications where microbial corrosion is a significant concern, such as in pipelines and marine environments.	MIC testing involves the integration of microbiological techniques, necessitating specialized expertise.

In summary, the selection of a corrosion testing method for green inhibitors depends on the

specific requirements of the application and the desired level of detail in the corrosion assessment. Integrating multiple methods often provides a more comprehensive understanding of the inhibitive performance of green corrosion inhibitors in diverse environments.

2.2.1 Electrochemical corrosion tests

Electrochemical corrosion tests are used to evaluate the corrosion behavior of materials by measuring their electrochemical response in a corrosive environment. These tests work on the principle that corrosion is an electrochemical process involving the transfer of electrons between a metal and its environment. The key methods include Tafel polarization, which measures the corrosion current to determine the corrosion rate, and electrochemical impedance spectroscopy (EIS), which evaluates the material's resistance to corrosion by analyzing its impedance over a range of frequencies. These techniques provide insights into the corrosion kinetics, inhibitor efficiency, and overall material durability.

The experimental setup for the electrochemical corrosion tests is shown in the following figure. A typical experimental setup for electrochemical corrosion tests consists of a three-electrode electrochemical cell connected to a potentiostat or galvanostat. As shown in Figure 1.5, the key components of this experimental setup are:

1). Working Electrode: The metal sample or material under investigation, usually in the form of a flat coupon, is used as the working electrode where corrosion occurs.

2). Reference Electrode: A stable electrode (silver/silver chloride electrode) that provides a constant potential for accurate measurement of the working electrode's voltage.

3). Counter Electrode: A conductive material, often platinum or graphite, used to complete the electrical circuit and allow current to flow through the electrolyte.

4). Electrolyte Solution: A corrosive medium that mimics the environment in which the material operates, such as a salt solution (e.g., 3.5% NaCl) or acidic solutions like HCl according to the literature for coupon level corrosion testing. It should be noted that this solution does not represent the realistic corrosive environments and is only used for screening purposes of inhibitors. The best performing inhibitor will be evaluated under the conditions which simulates real gas pipeline components once the screening is finished

5. Potentiostat/Galvanostat: An electronic device that controls the potential (in potentiostatic mode) or current (in galvanostatic mode) between the working and reference electrodes, allowing for the monitoring of corrosion rates and other electrochemical parameters. The model number of our potentiostat is VersaSTAT 4 manufactured by Princeton Applied Materials.

6. Test Chamber: The electrochemical cell is typically housed in a temperature-controlled chamber to maintain a constant experimental environment, ensuring repeatability. Most of our tests are carried out at ambient temperatures.

In this setup, the working electrode is exposed to the corrosive environment while the potentiostat measures and controls the electrochemical reactions, providing detailed data on corrosion mechanisms, inhibitor performance, and material degradation.

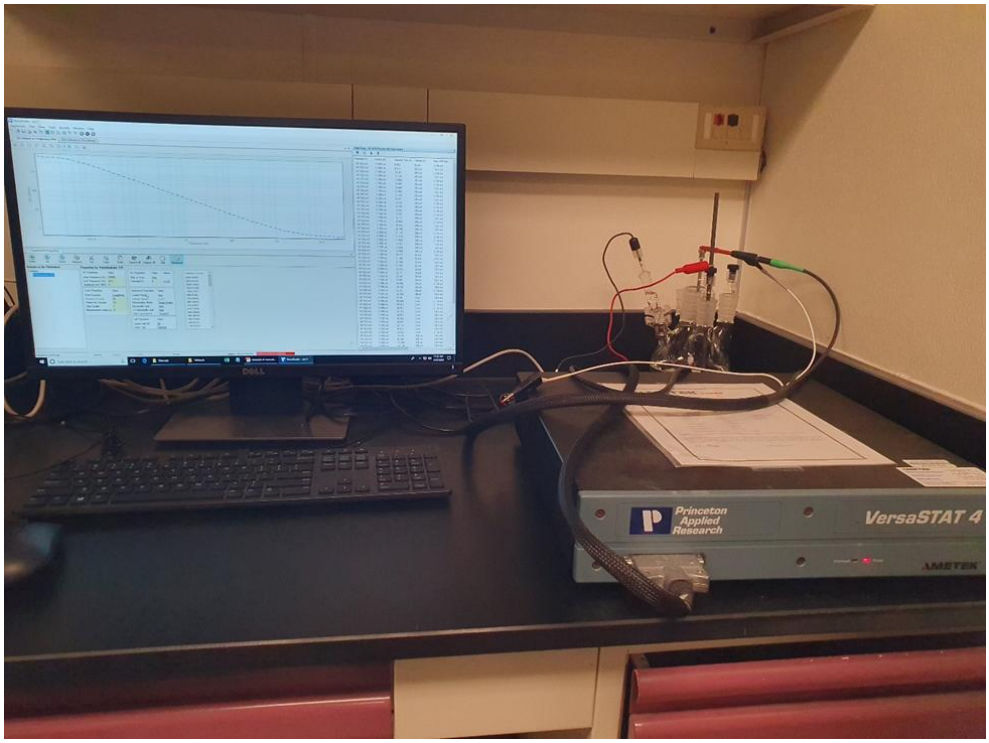

Figure 1.5. Electrochemical corrosion test setup

2.2.1.1 Tafel polarization method

Tafel polarization, a cornerstone of electrochemical analysis, plays a critical role in assessing the durability and lifespan of metals under corrosive conditions. This technique, based on Tafel extrapolation, provides vital insights into the corrosion mechanisms of metals, making it

indispensable in fields ranging from infrastructure engineering to the development of marine vessels.

The method derives its name from Julius Tafel, who, in the early 20th century, first described the relationship between the overpotential and the logarithm of the current density during electrochemical reactions. This foundational work laid the groundwork for using these relationships to probe the kinetics of electrochemical reactions, particularly corrosion processes.

Corrosion, an electrochemical phenomenon, involves the deterioration of materials due to interactions with their environment. In metals, this typically manifests as the oxidation of metal atoms, which lose electrons and form ions. The susceptibility of metals to corrosion depends on their environment and material properties, posing significant risks to their structural integrity and functionality.

In practical terms, Tafel polarization allows engineers and scientists to quantitatively measure the rate of corrosion using the corrosion current density derived from Tafel plots. These plots graph the potential versus the logarithm of the current density, revealing key information about the anodic and cathodic reactions that occur on the surface of the electrode.

The significance of Tafel polarization extends beyond simple measurement. The technique is critical for:

- **Material Selection and Design**: Helping select materials with better corrosion resistance for specific applications.
- **Corrosion Inhibitor Evaluation**: Testing the efficacy of various corrosion inhibitors to find the most effective compounds for protecting metals.
- **Predictive Maintenance and Life Prediction**: Providing data that aid in forecasting the need for maintenance or replacement of corroded components, thereby averting potential breakdowns.

Technical Overview of the Tafel Polarization Method

Technically, the Tafel polarization test involves several steps, starting with the measurement of the open circuit potential (OCP) to establish a baseline for the electrochemical system at equilibrium. The subsequent application of varying potentials helps map out the complete electrochemical behavior of the test material, capturing phenomena like passivation or activation that are critical to understanding its corrosion behavior.

During the test, both anodic (oxidation) and cathodic (reduction) reactions are explored. The anodic reaction involves the metal losing electrons, while the cathodic reaction involves the gain of electrons. The slopes of the lines in the Tafel plot, known as Tafel slopes, are indicative of the energy barriers for these reactions. Accurately determining these slopes is crucial for extrapolating the corrosion current density (i_{corr}), which directly correlates to the metal's corrosion rate. Figure 1.6 shows the Tafel plot and measured corrosion parameters.

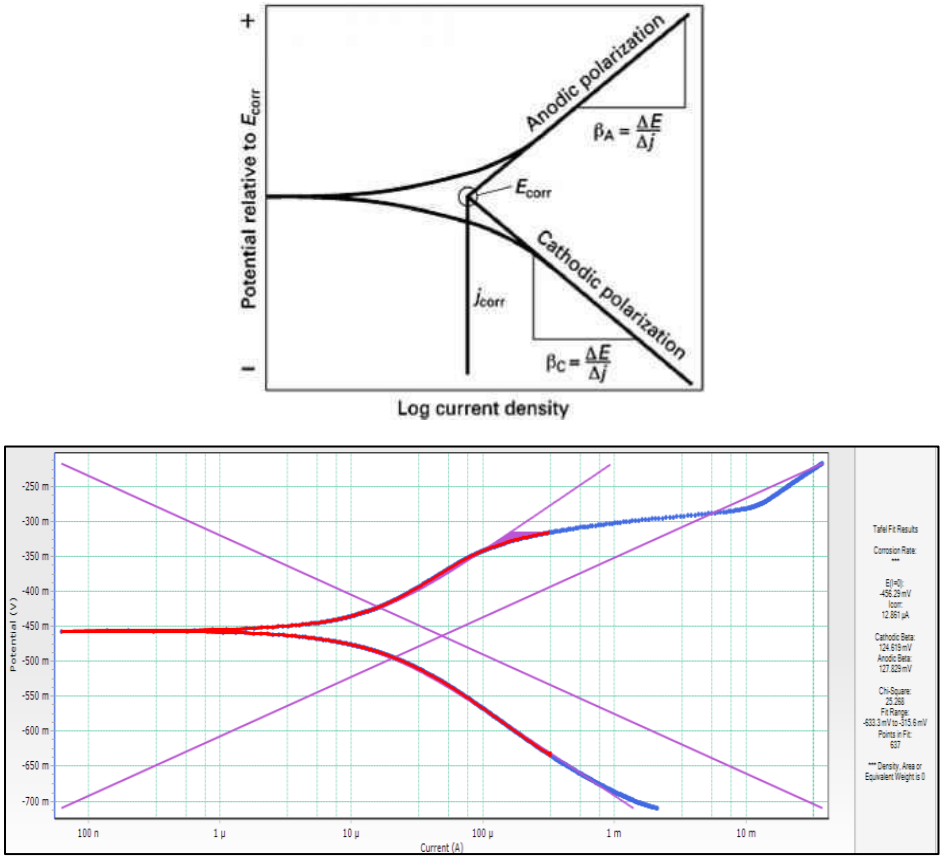

Figure 1.6 Graphical Representation of the Tafel Polarization Corrosion Test Results

A detailed analysis of the Tafel plot allows researchers to pinpoint the corrosion potential where the anodic and cathodic currents balance, a key metric in evaluating the stability of the metal in its operational environment. The intersection point of the extrapolated anodic and cathodic Tafel lines provides a precise measure of the corrosion rate, which is essential for assessing the protective qualities of corrosion inhibitors and the overall resilience of the metal.

Thus, Tafel polarization is more than just a testing method; it is a comprehensive approach that offers a deep understanding of corrosion processes. This knowledge is crucial for developing

strategies to mitigate corrosion, enhance material performance, and ensure the longevity and safety of metal components across various industries.

Procedures for Conducting the Tafel Polarization Test

Equipment Setup and Preparation

For the Tafel polarization test, a controlled electrochemical setup was utilized, typically comprising a potentiostat, a three-electrode cell, and software for data acquisition and analysis. The three-electrode system consisted of a working electrode (the metal under test), a reference electrode, and a counter electrode.

Stabilization of Open Circuit Potential (OCP)

The metal sample was immersed in the test solution, and the system was allowed to equilibrate to the open circuit potential (OCP). This step was crucial as it established a stable baseline condition for the electrochemical system. The OCP is the potential where the net current at the electrode surface is zero, indicating that the rates of the anodic and cathodic reactions have reached equilibrium.

Test Medium Preparation

To assess the impact of pectin as a corrosion inhibitor on A36 steel, low-carbon steel used in the manufacturing of gas pipelines, two distinct media were prepared:

- **Medium 1 (Control):** A pure 1M HCl or 3.5 % NaCl solution served as the control to assess the corrosion impact on unprotected A36 steel in a highly corrosive environment.
- **Medium 2 (Pectin Mixed):** A 1M HCl or 3.5% solution containing 2g of pectin per liter of medium. This medium aimed to investigate the protective effects of pectin against steel corrosion in acidic conditions. Other inhibitors can be applied on the metal surface either in a solution or by dip-coating. More details can be found in results and discussion sections.

Test Parameter Configuration

The configuration of the test parameters was performed through the software interface of the potentiostat. Key parameters entered included:

- **Initial Potential ($E_{initial}$)**: Set 10 mV negative relative to the OCP. This was the starting point for the potential sweep.
- **Final Potential (E_{final})**: Set 10 mV positive relative to the OCP. This defined the endpoint of the potential sweep.

- **Scan Rate**: Determined to be approximately 0.125 mV/s. The scan rate was crucial for ensuring that the system did not deviate significantly from equilibrium during the test.

Execution of the Potentiodynamic Polarization Test

Once the parameters were set, the potentiodynamic polarization test was initiated. The software controlled the potentiostat to apply a linear sweep of potential from the initial to the final set values. During this sweep:

- The potential was incrementally increased from $E_{initial}$ to E_{final}.
- The current response of the system was continuously measured as the potential was varied.

Data Acquisition and Plotting

The current and potential data collected during the tests were automatically recorded by the software. This data was used to generate the Tafel plot, which graphed the potential (E) on the Y-axis versus the logarithm of the current density (log I) on the X-axis. The Tafel plot was essential for analyzing the electrochemical behavior of the metal under the test conditions.

Identification of Linear Regions and Extrapolation

The Tafel plot typically exhibited linear regions corresponding to the anodic and cathodic branches. These regions were critical for the analysis as they reflected the kinetics of the oxidation and reduction reactions. Using the software:

- The linear portions of the anodic and cathodic curves were identified.
- These linear regions were extrapolated back to their intersection at the corrosion potential (E_{corr}).

Calculation of Corrosion Current Density (i_{corr})

The intersection point of the extrapolated anodic and cathodic lines provided the value of the corrosion current density (icorr). This value was crucial as it directly related to the corrosion rate of the metal. The software facilitated the conversion of icorr into the corrosion rate using pre-defined constants and material properties such as the equivalent weight of the metal and its density. Finally, the corrosion rate (CR) and efficiency of pectin on inhibition of corrosion (IE) were calculated using the following formulas.

$$CR = \frac{Icorr.K.EW}{\rho.A} \qquad (1)$$

$$IE = \frac{CR_{pectin} - CR_{control}}{CR_{control}} \times 100 \quad (2)$$

Where:

CR = Corrosion rate

IE= inhibition efficiency

k= Constant that depends on the units used for corrosion rate

Icorr = Corrosion current density (A/cm^2)

EW = Equivalent weight of the corroding metal

ρ = Density of the metal (g/cm^3)

A = Exposed surface area of the metal (cm^2)

2.2.1.2 Electrochemical impedance spectroscopy method

Electrochemical Impedance Spectroscopy (EIS) is a powerful and sensitive analytical technique widely used in the field of electrochemical corrosion testing. By measuring the impedance of a system over a range of frequencies, EIS provides detailed insights into the electrochemical processes occurring at the interface between a metal and its environment. This methodology has become indispensable for researchers and engineers involved in the development of corrosion-resistant materials and the assessment of protective coatings.

The theoretical foundation of EIS is rooted in the early 20th-century developments in electrochemistry and electrical engineering. However, it was not until the advent of modern electronics and computers in the latter half of the century that EIS evolved into the sophisticated tool it is today. Initially used for studying battery systems and fuel cells, the application of EIS in corrosion science began to gain prominence as it provided a non-destructive means of analyzing corrosion mechanisms.

Principles of EIS

Electrochemical Impedance Spectroscopy operates on the principle of applying a small amplitude AC voltage to an electrochemical cell and measuring the resulting current. The response of the system is analyzed across a spectrum of frequencies to determine the impedance, a complex quantity comprising resistive and reactive (capacitive and inductive) elements. The impedance of a metal/environment interface is influenced by various factors, including the properties of the metal, the nature of the electrolyte, and the presence of any corrosion products or coatings.

Advantages of EIS in Corrosion Testing

EIS offers several advantages over traditional corrosion testing methods:

- **Non-Destructive**: EIS does not alter the sample during testing, allowing for real-time monitoring of corrosion processes.
- **Sensitivity to Surface Changes**: EIS can detect minute changes in the electrochemical properties of the interface, making it ideal for evaluating the effectiveness of corrosion inhibitors and coatings.
- **Wide Range of Applications**: From monitoring corrosion in reinforced concrete to assessing the integrity of coatings on aircraft, EIS's versatility makes it a valuable tool across diverse industries.

EIS Data Interpretation

The interpretation of EIS data is typically facilitated through the use of Nyquist and Bode plots, which graphically represent the impedance characteristics of the system. These plots can reveal:

- **Charge Transfer Resistance**: Related to the ease with which electrons can move across the electrode/electrolyte interface.
- **Double Layer Capacitance**: Reflects the capacitive behavior at the interface, influenced by the thickness and properties of the electrochemical double layer.
- **Warburg Impedance**: Indicates diffusion-controlled processes, often seen in porous coatings or corrosion layers.

Applications in Corrosion Science

In corrosion science, EIS is used to study:

- **Corrosion Kinetics**: Understanding how the corrosion rate changes with time under various environmental conditions.
- **Evaluation of Corrosion Inhibitors**: Assessing how different inhibitors affect the electrochemical behavior of the metal.
- **Coating Degradation**: Monitoring the degradation of protective coatings over time to predict failure and maintenance needs.

Methodology for Electrochemical Impedance Spectroscopy

Electrochemical Impedance Spectroscopy (EIS) tests were conducted to evaluate the efficacy of pectin as a corrosion inhibitor on A36 steel. These tests were performed in two different media:

- **Medium 1 (Control)**: Pure 1M HCl or 3.5% NaCl solution.

- **Medium 2 (Pectin Mixed)**: A 1M HCl or 3.5% NaCl solution containing 2g of pectin per liter of medium.

The EIS measurements utilized a standard three-electrode cell setup:

- **Working Electrode**: A36 steel specimen with polished surface using sand #80, #200, #400, #800, #1200. The sample surface was polished as per test protocol for higher accuracy of corrosion test results.
- **Reference Electrode**: Saturated Calomel Electrode (SCE).
- **Counter Electrode**: Platinum wire.

Instrumentation and Measurement Parameters

The EIS was conducted using a frequency response analyzer coupled with a potentiostat, which maintained the electrode potential and measured the impedance response. The specific parameters used in the EIS tests are summarized in the table below:

Table 1.3 Parameters used in the EIS tests

Parameter	Value	Description
AC Signal Amplitude	10 mV	The amplitude of the alternating current signal.
Frequency Range	100 kHz to 10 mHz	The range over which impedance was measured.
Potentiostat Mode	Potentiostatic (constant potential)	Maintains a constant electrode potential during measurements.
Equilibration Time	At least 3 hours	Allows the system to stabilize before measurements.

Data Acquisition

EIS measurements were initiated after a stabilization period, during which the electrochemical system reached a steady state. Impedance data were acquired across the specified frequency range, capturing the complete electrochemical response.

Data Analysis

The impedance data were analyzed by fitting them to an equivalent circuit model to extract key parameters such as solution resistance (Rs), charge transfer resistance (Rct), and constant phase element (CPE). These parameters were derived from Nyquist plots, which graph the imaginary part of impedance (Z'') against the real part (Z').

Equivalent Circuit Model

The equivalent circuit used for analyzing the impedance plots consisted of:

Figure 1.7. Equivalent Circuit Diagram Derived from EIS Corrosion Test Results

- **R1**: Solution resistance (R_s).
- **R2**: Charge transfer resistance (R_{ct}).
- **CPE1**: Impedance of the constant phase element.

Steps for Measuring Solution and Charge Transfer Resistance

1. **Perform EIS Measurement**: Conduct an EIS experiment over a broad frequency range.
2. **Analyze Nyquist Plot**: Plot the Nyquist diagram and identify the intercepts and features corresponding to R_s and R_{ct}.
3. **Calculation of Parameters**:
    - **Solution Resistance (R_s)**: High-frequency intercept on the real axis of a Nyquist plot.
    - **Charge Transfer Resistance (R_{ct})**: Represents the electron transfer resistance at the electrode-electrolyte interface.

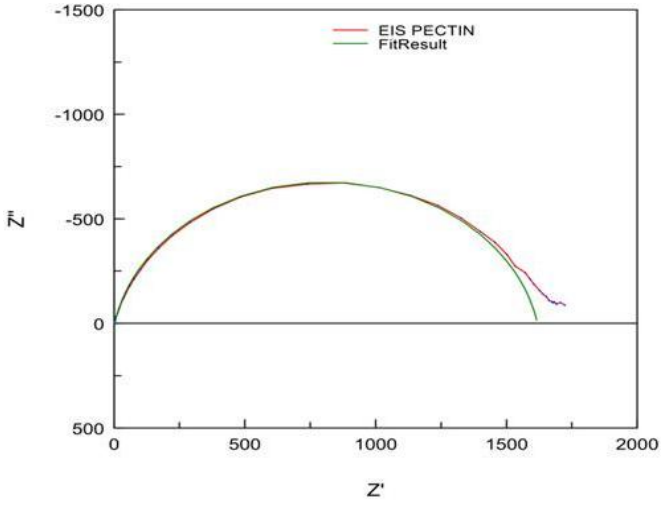

Element	Freedom	Value	Error	Error %
R1	Free(±)	1.916	0.059769	3.1195
CPE1-T	Free(±)	7.2283E-05	3.7447E-06	5.1806
CPE1-P	Free(±)	0.88668	0.0075996	0.85708
R2	Free(±)	1616	39.3	2.4319

Figure 1.8. Nyquist diagram of electrochemical impedance spectroscopy test

The impedance characteristics, such as the diameters of the semicircles in Nyquist plots, indicate the corrosion resistance. An increased diameter implies higher corrosion resistance and is a direct measure of the inhibitory effects of pectin. The results were quantitatively assessed using the collected EIS parameters, specifically focusing on the changes in Rs and Rct, to evaluate the performance of pectin as a corrosion inhibitor.

This systematic approach provided a comprehensive understanding of the corrosion behavior of A36 steel in the presence and absence of pectin, underlining the effectiveness of EIS in evaluating corrosion inhibitors in various media. The following formula was used to measure pectin's inhabitation efficiency (IE).

$$IE = \frac{R_{P\ Pectin} - R_{P\ Control}}{R_{P\ Control}} \quad (3)$$

2.2.2 Static corrosion weight loss experiments

We have conducted long-term weight loss tests to evaluate the sustainability and corrosion protection capabilities of pectin over extended periods. The corrosion tests employed A36 steel sheets, characterized by an unpolished (mill) finish, hot rolled, and conforming to ASTM A36 standards. The steel sheets, with a thickness of 0.06 inches, were cut using a CNC cutter into test coupons measuring 2.0 cm by 1.0 cm. A corrosive medium was prepared using 1M hydrochloric acid (HCl), formulated from 37 percent analytical reagent (AR) grade HCl. This solution aimed to simulate aggressive corrosion conditions. A brine water medium of 3.5% NaCl that mimics the seawater salt concentration can be prepared by dissolving NaCl salt in water. Two distinct mediums were prepared to evaluate the corrosion resistance of the steel coupons under varying conditions:

Medium 1 (Control): Pure 1M HCl or 3.5% NaCl brine solution, serving as the control to assess the effect of the corrosive medium on unprotected A36 steel.

Medium 2 (Pectin Mixed): A solution consisting of 0.2 g of pectin dissolved in 100 ml of water, mixed with pure 1M HCl or 3.5% NaCl solution. This medium aimed to investigate the influence of pectin presence in the corrosive media on steel corrosion.

The differences in weight loss across the two media were analyzed to assess the efficacy of pectin and other inhibitors in mitigating corrosion on A36 steel.

Test Procedure

For each test, the respective steel coupons were completely immersed in a 500 ml glass beaker containing one of the prepared test solutions. The experiments were conducted over several durations of 2 weeks, 4 weeks, and 6 weeks at a controlled temperature of 25 °C. To minimize the influence of oxygen and ensure consistent conditions, the beakers were placed in a fume hood. Before immersion, each steel coupon was accurately weighed to determine its initial mass. Following the exposure periods, the coupons were retrieved from their respective solutions. To remove any corrosion products formed during the test, each coupon was thoroughly scrubbed under running water using a bristle brush and cleaned with acetone. After cleaning, the coupons were dried in acetone to remove any residual moisture and reweighed to determine the final mass.

Field Testing: None

3. Results and Discussions

3.1 Task 1: Design and Synthesis of Multi-compound Green Inhibitors

3.1.1 Task 1.1: Quick Screening of Green Inhibitors for Gas Pipeline Protection

We have completed an extensive literature review to identify green inhibitors suitable for corrosion protection in gas pipelines. Conducting a comprehensive literature review was a key step in our project of developing green inhibitors tailored for gas pipeline protection. This extensive exploration involved investigating a vast body of existing research and scholarly works to identify potential candidates with inhibitive properties. The objective was to discern promising organic compounds and extracts known for their corrosion-resistant capabilities, with a particular focus on those derived from renewable sources. By synthesizing knowledge from diverse scientific publications, we aimed to gain insights into the latest advancements, challenges, and trends in the field of green inhibitors for corrosion protection.

The literature review not only facilitated the identification of potential inhibitor candidates but also provided a holistic understanding of the various mechanisms and factors influencing corrosion inhibition. This knowledge base proved instrumental in guiding subsequent research activities and refining our approach to the synthesis of green inhibitors. Furthermore, insights garnered from the literature review informed our decisions regarding the selection of inhibitor candidates that not only demonstrated robust inhibitive properties but also aligned with the principles of sustainability and environmental consciousness. As we move forward with our research, the outcomes of this comprehensive literature review serve as a crucial reference point for shaping the direction and focus of our investigation into innovative solutions for gas pipeline corrosion protection.

In this subtask, our investigation has highlighted the efficacy of organic compounds containing nitrogen, oxygen, and/or sulfur as formidable industrial corrosion inhibitors. These synthetic organic inhibitors exhibit the capability to create a protective layer between the metal surface and the corrosive environment, thereby slowing down the process of metal disintegration through an adsorption mechanism. However, a significant drawback lies in the often-exorbitant cost and toxic nature of these synthetic counterparts. The disposal of such industrial corrosion inhibitors further compounds environmental concerns, necessitating a shift toward more sustainable practices.

Recognizing the escalating demand for environmentally friendly alternatives, there is a growing inclination toward green-based inhibitors. These inhibitors, derived from sources like plant extracts and microbial enzymes, present a compelling solution. Their inherent non-toxic nature positions them as preferable options compared to their commercial counterparts. Notably, plant extracts and microbial enzymes are regarded as green and sustainable materials due to their natural and biological properties. These compounds demonstrate the ability to effectively inhibit the corrosion of metals and alloys. Among these, the leaves stand out as a particularly advantageous source, as they boast an abundance of phytochemicals—active components synthesized by the plant—mimicking the performance of commercial inhibitors. This shift toward green and sustainable materials reflects a conscientious effort to address both environmental and economic considerations in the realm of corrosion inhibition.

Table 1.4 Examples of bio-based corrosion inhibitors to be investigated in this project.

Plant or Source	Active Constituent	Solvent & extraction method	Metal to Protect	Corrosive Environment	Corrosion Inhibition Efficiency (%)	Inhibitor Concentration
Citrus peel	Pectin	HCl and ethanol	Mild steel	1M HCl	94.2 at 45 °C	2 g L-1
Shrimps shell waste	Chitosan	NaOH	Carbon steel	1M HCl	88.5 at 25 °C	10-5 M
Plantago ovata	Polysaccharide (galaturonic acid)	Water	A1020 carbon steel	1M HCl	94.4 at 45 °C	1 g L-1
Rhododendron schlippenbachii	Polyphenolic compounds	Methanol	Low carbon steel	1M H2SO4	94.2 at 30 °C	600 ppm

Building on the screening results from Task 1.1, we propose the production of four bio-based corrosion inhibitors, as detailed in Table 1.4. The primary objective is to optimize polarization resistance and minimize corrosion current, aiming for robust protection of pipelines.

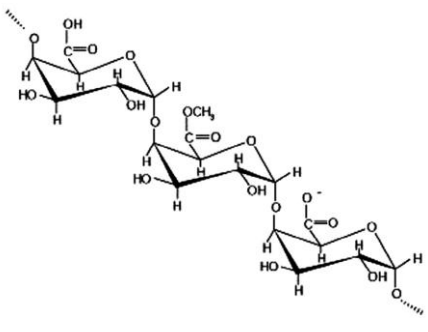

Figure 1.9. Molecular structure of pectin

To extract pectin, we employed a systematic process using fresh citrus peels obtained from citrus unshiu

marcovitch, sourced from a local citrus producer in Mesa, Arizona. The resultant natural pectic polysaccharides, primarily comprising homogalacturonan, rhamnogalacturonan I and II, and xylogalacturonan, possess a molecular structure illustrated in Figure 1.9.

Key functional groups such as OH-, C=O, and C-O in pectin are pivotal in generating an attractive force for its adhesion to the metal surface. This mechanism effectively prevents reactive fluids from directly contacting the metal surface, thereby enhancing the inhibitor's capacity to safeguard against corrosion in pipeline systems. The careful extraction and utilization of pectin from citrus peels highlights our commitment to leveraging sustainable and effective green corrosion inhibitors for enhanced pipeline protection.

The synthesis of nitrogen-containing green inhibitors from biomass presents a highly desirable yet challenging endeavor. In our approach, we made these inhibitors using chitosan derived from shrimp shells, along with cinnamyl aldehyde, vanillic aldehyde, citral, and anisaldehyde. Chitosan, sourced from shrimp shells collected in local restaurants, serves as a widely distributed but recyclable green resource, albeit with a high production cost. Its distinct molecular structure positions chitosan derivatives as effective and environmentally friendly corrosion inhibitors for gas pipelines. The molecular structures of the four inhibitors, depicted in Figure 1.10, have been meticulously synthesized following established procedures.

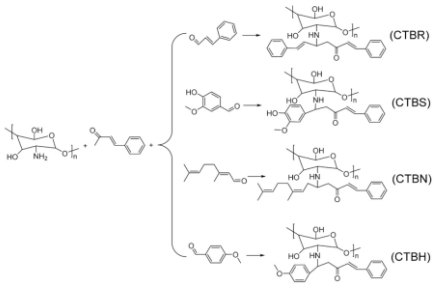

Figure 1.10. Synthetic route to four inhibitors

Carbohydrate polymers, known for their chemical stability, biodegradability, and eco-friendliness, stand out as key macromolecules in corrosion inhibition. Derived from Plantago husk, these polymers offer an inexpensive, renewable, and abundantly available alternative. The hydroxyl group (OH) and heteroatom oxygen in polysaccharides facilitate their adsorption onto metal surfaces, contributing to corrosion prevention. The extraction process involves soaking Plantago husk in distilled water for 48 hours, followed by boiling to release mucilage. After filtration to remove insoluble husks, an equal volume of acetone is added to precipitate the polysaccharide, which is then dried, powdered, and stored.

For biodegradable green inhibitors derived from *Rhododendron schlippenbachii*, rich in phenolic compounds, a modification in the extraction process is proposed. The traditional

methanol extraction method will be replaced with water as the solvent, and the leaf extracts will undergo purification before application to metal surfaces. Initial studies indicate a noteworthy 94.2% corrosion inhibition efficiency when applying 600 ppm of this green inhibitor to low-carbon steel specimens. This comprehensive approach underscores our commitment to exploring sustainable and effective green inhibitors, leveraging diverse biomass sources and extraction methods for enhanced corrosion protection.

3.1.2 Task 1.2: Synthesis and Characterization of Green Inhibitors from Renewable Feedstock

We have explored various methods for converting citrus peel into pectin, optimizing it as a green inhibitor for gas pipeline protection. Our detailed study focused on refining the extraction and synthesis processes of pectin from orange peels. Additionally, we developed techniques to chemically modify pectin, enhancing its corrosion resistance through cross-linking and optimizing its adhesion properties for improved performance in harsh environments.

To further enhance pectin's inhibition efficiency, we investigated methods to increase its adsorption on metal surfaces by incorporating additional active functional groups using EDC (1-Ethyl-3-(3-dimethylaminopropyl)carbodiimide) and NHS (N-Hydroxysuccinimide). We also initiated preliminary research on extracting and synthesizing chitin and chitosan from shrimp shells, identifying them as promising green corrosion inhibitors.

3.1.3 Task 1.3: Corrosion Testing for Verification and Validation

3.1.3.1 Electrochemical corrosion test result

3.1.3.1.1 Tafel polarization in 1M HCl solution

The Tafel polarization tests, carried out in two separate media, revealed unique corrosion properties for A36 steel, thereby highlighting the effectiveness of pectin as a corrosion inhibitor. The results of these tests produced Tafel plots, from which crucial parameters like corrosion potential (Ecorr), corrosion current density (icorr), and corrosion rate were extracted. The raw data from the Tafel plots indicated the following outcomes for each medium:

Table 1.5 Raw data from the Tafel plots for each medium

Medium	E_{corr} (mV)	i_{corr} (μA/cm²)	CR (mmpy)	Inhibition Efficiency
1M HCl (Control medium)	-453.05	18.94	0.219	N/A

1M HCl+2g/L pectin	-456.29	12.86	0.1487	32%

The comparative analysis of the data from the two media reveals a clear decrease in both the corrosion current density and the corrosion rate in the presence of pectin. Specifically, the incorporation of pectin resulted in a reduction of icorr by approximately 32%, indicating a significant decrease in the rate at which corrosion progressed.

The effectiveness of pectin as a corrosion inhibitor can be attributed to its ability to form a protective barrier on the metal surface. This barrier likely impedes the access of corrosive agents (HCl ions) to the steel surface, thereby reducing the electrochemical reactions that lead to corrosion. The slight shift in corrosion potential (Ecorr) in the presence of pectin (from -453.05 mV to -456.29 mV) supports the notion that pectin modifies the electrochemical environment at the steel surface.

The results underscore the potential of pectin as a viable, environmentally friendly corrosion inhibitor for A36 steel in acidic environments. The 32% inhibition efficiency indicates a substantial protective effect, which could translate into significantly increased lifespan and reduced maintenance costs for steel structures.

The Tafel polarization tests demonstrated the efficacy of pectin as a corrosion inhibitor. The significant reduction in corrosion rate and the alteration in electrochemical behavior of the steel surface suggest that pectin or similar organic inhibitors could play an essential role in corrosion protection strategies, particularly in industries where steel is exposed to acidic conditions. Further research could explore the molecular interactions between pectin and metal surfaces to optimize the formulation and application methods for industrial use.

3.1.3.1.2 Tafel polarization in 3.5% NaCl solution

We have established a performance baseline using industry-standard chemical inhibitors to benchmark and compare the effectiveness of green inhibitors. To evaluate the efficacy of chemical amines and pectin-based green inhibitors in mitigating corrosion, comprehensive electrochemical tests and static weight loss assessments were conducted on A36 metal coupons. These tests were carried out in a corrosive medium consisting of a 3.5% NaCl solution at 25°C, without any corrosion inhibitors, to establish a control benchmark. This study focused on the

performance of pectin, both as a solution and as a coating on the metal surface, alongside three chemical amines—monosisopropanolamine, N-methyldiethanolamine, and monoethanolamine.

The Tafel polarization tests that were carried out in seven separate media revealed unique corrosion properties for A36 steel, thereby highlighting the effectiveness of pectin and amines as corrosion inhibitors. The results of these tests produced Tafel plots, from which crucial parameters like corrosion potential (Ecorr), corrosion current density (icorr), and corrosion rate were extracted. The raw data from the Tafel plots indicated the following outcomes for each medium.

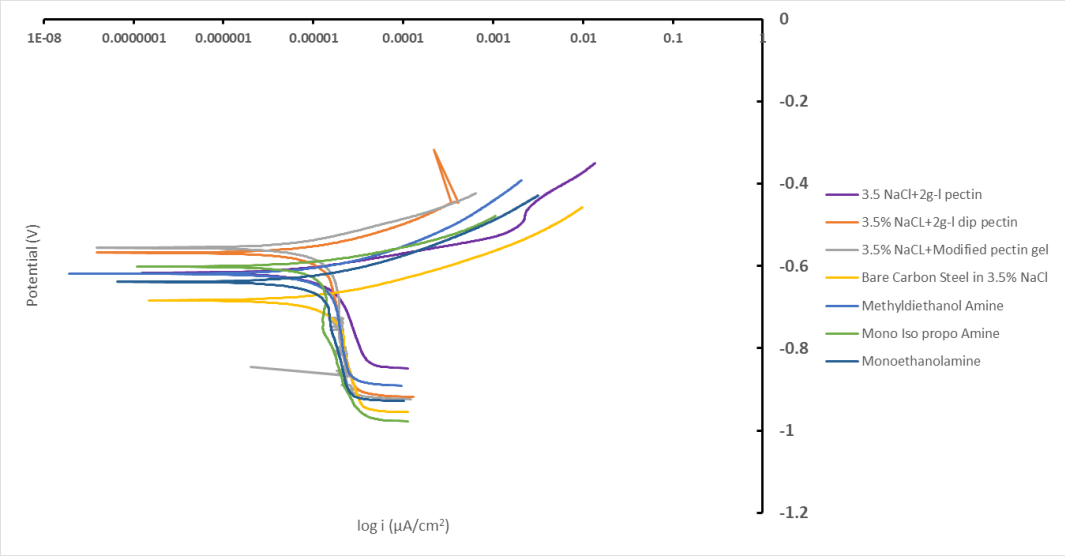

Figure 1.11 Graphical representation of the Tafel polarization corrosion test results

Table 1.6 Raw data from the Tafel plots for each medium

Sample	E_{corr} (mV)	Icorr (µA/cm²)	CR (mmpy)	Inhibition efficiency (%)
Bare Carbon Steel in 3.5% NaCl	-683.5	22.6	0.261	-------
3.5 NaCl+2g-l pectin	-616.7	14.2	0.164	37.2%
3.5% NaCl+2g-l dip pectin	-567.8	7.46	0.086	67.0%
3.5% NaCl+ modified pectin gel	-555.7	7.34	0.0849	67.5%
N-methyldiethanol amine	-619.2	9.75	0.113	57.1%
Monoisopropanol amine	-601.4	9.74	0.113	56.9%
Monoethanolamine	-638.2	14.4	0.167	36.3%

The Tafel polarization data provides insight into the corrosion resistance of both pectin-based inhibitors and amines, supporting the findings from the EIS analysis. Bare carbon steel in 3.5% NaCl shows the highest corrosion current density (Icorr) at 22.6 µA/cm², indicating no inhibition and the highest corrosion rate. When 3.5% NaCl + 2g-I pectin is introduced, the Icorr

drops to 14.2 μA/cm², yielding a modest inhibition efficiency of 37.2%, suggesting some adsorption of pectin molecules onto the steel surface, which slows the corrosion process.

The performance significantly improves with 3.5% NaCl + 2g-I dip pectin, which shows an Icorr of 7.46 μA/cm² and an inhibition efficiency of 67.0%. This indicates a stronger adsorption and a more effective barrier against corrosion. The modified pectin gel provides the best performance, with the lowest Icorr at 7.34 μA/cm² and the highest inhibition efficiency of 67.5%. This result demonstrates that the modified pectin forms an excellent protective layer on the steel surface, significantly reducing the corrosion rate and shifting the corrosion potential in a more positive direction, further confirming its high efficacy.

Amines are included in our studies to benchmark the performance of green corrosion inhibitors. We evaluated a range of amines recommended by our industrial advisory board, particularly those suggested by our technical advisory panel (TAP) members. Amines vary in their mechanisms of action based on their chemical structure and application methods. Some work well in continuous dip applications by forming protective films on metal surfaces, while others are more effective in batch treatments, interacting with corrosive agents over time.

In establishing a baseline for comparing green inhibitors, we assessed traditional amine-based inhibitors. N-methyldiethanol amine and mono isopropyl amine showed good corrosion protection, with Icorr values of 9.75 μA/cm² and 9.74 μA/cm², resulting in inhibition efficiencies of about 57%. These amines create protective layers on steel surfaces, reducing corrosion rates. Conversely, monoethanolamine had a higher Icorr of 14.4 μA/cm² and a lower efficiency of 36.3%, making it the least effective of the tested amines, although it still provides some protection.

Our main goal is to investigate the efficiency of green inhibitors, despite the corrosion protection offered by traditional inhibitors. We will compare their effectiveness and emphasize their environmental benefits. We understand that extensive testing of amines may affect the budget and timeline, and we will work with experts (e.g., TAP members) and plan accordingly to balance the testing of both amines and green inhibitors.

3.1.3.1.3 EIS results obtained in 1M HCl solution

EIS tests were performed on A36 steel in both control and pectin-infused media, yielding important impedance data. These data were examined using Nyquist plots. The findings underscore substantial variations in the electrochemical behavior of the steel when the pectin inhibitor is present versus when it is absent.

Interpretation of Nyquist Plots

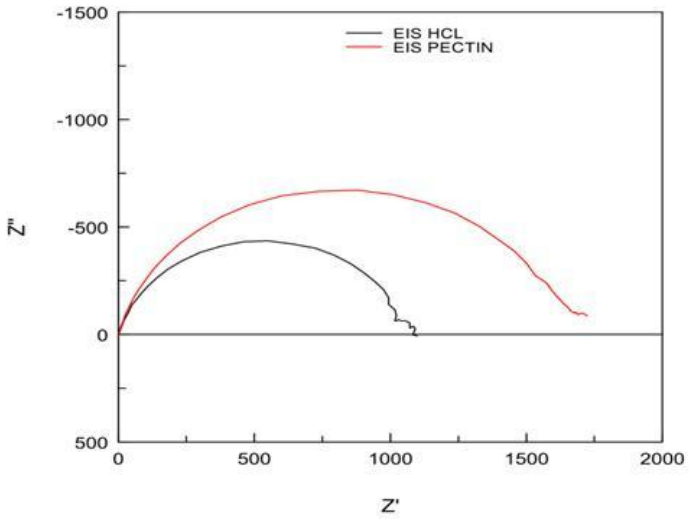

Figure 1.12. Comparative Nyquist Plots for Both Media

Nyquist plots for both media displayed a single semi-circle, indicative of a charge-transfer controlled corrosion process. The key observations from the Nyquist plots include:

- **Uninhibited Solution (Control)**:
    - Smaller black semi-circle diameter in Fig. 1.12, indicating lower impedance values.
- **Inhibited Solution (Pectin Mixed)**:
    - Larger red semi-circle diameter in Fig. 1.12, suggesting increased impedance and thus enhanced resistance to corrosion.

These observations imply that the presence of pectin at the carbon steel-electrolyte interface increases the impedance, thereby reducing the corrosion rate.

Quantitative Analysis

The EIS parameters extracted from the equivalent circuit model provided quantitative insights into the corrosion inhibition mechanism:

Table 1.7 EIS parameters extracted from the equivalent circuit model

Parameter	Control	Pectin Mixed	Unit	Improvement with Pectin
Solution Resistance (Rs)	2.1	1.9	Ω cm²	Increased conductivity
Polarization Resistance (Rct)	1046	1616	Ω cm²	Improved by 54.5%
Constant Phase Element (CPE)	9.9×10^{-5}	7.2×10^{-5}	F/s	Reduced capacitance
Inhibition Efficiency	-	54	%	Significant improvement

Key Observations:

- **Solution Resistance (Rs)**: A slight decrease in Rs in the pectin mixed solution indicates slightly better ionic conductivity.
- **Polarization Resistance (Rct)**: A significant increase in Rct from 1046 Ω cm^2 in the control to 1616 Ω cm^2 in the pectin mixed solution suggests a substantial improvement in corrosion resistance due to the inhibitory action of pectin.
- **Constant Phase Element (CPE)**: The decrease in CPE value reflects a reduction in the double-layer capacitance, possibly due to the formation of a more compact layer at the electrode surface.

The enhanced polarization resistance in the presence of pectin indicates that pectin molecules adsorb onto the steel surface, forming a protective barrier that impedes the charge transfer process associated with corrosion. This barrier effect not only increases the overall impedance but also modifies the electrochemical environment at the interface, making the corrosion process less favorable.

The slight imperfections in the semi-circle shape observed in the Nyquist plots, indicative of frequency dispersion, could be attributed to the roughness and heterogeneity of the metal surface. Such imperfections are typical in real-world scenarios and underscore the complexity of interpreting EIS data in practical corrosion systems.

So, the EIS test results convincingly demonstrate the effectiveness of pectin as a corrosion inhibitor in acidic environments. The quantitative data from the impedance analysis corroborate the visual and qualitative interpretations from the Nyquist plots, providing a comprehensive picture of the inhibitory mechanism. These findings not only validate the use of pectin as an eco-friendly corrosion inhibitor but also illustrate the utility of EIS as a diagnostic tool in the study of corrosion processes and inhibitor performance.

3.1.3.1.4 EIS results obtained in 3.5% NaCl solution

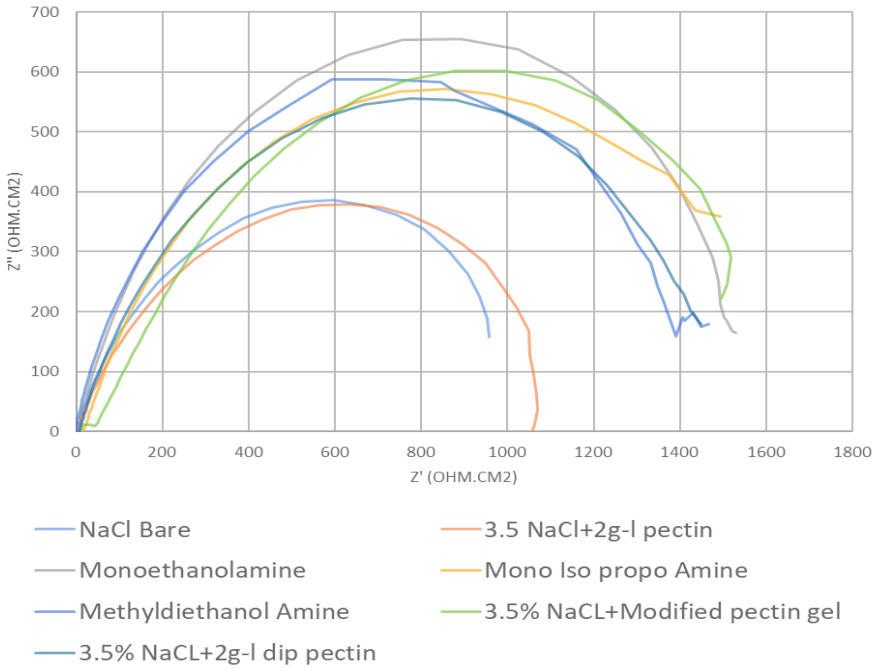

Figure 1.13. Comparative Nyquist plots for various inhibitors

Key Observations:

The 3.5% NaCl + modified pectin gel sample (green curve) shows the largest semicircle, indicating the highest corrosion resistance among all tested inhibitors.

In contrast, the bare carbon steel in NaCl (blue curve) has a much smaller semicircle, which confirms the lowest corrosion resistance in the absence of inhibitors.

Methyldiethanolamine (grey curve) and monoethanolamine (light blue curve) exhibit moderate-sized semicircles, signifying intermediate corrosion resistance

In EIS analysis, the polarization resistance (Rp) represents the diameter of the semicircle in Nyquist plots, where a larger Rp indicates higher corrosion resistance. The bare carbon steel has the smallest Rp value (1047 Ω cm^2), indicating poor corrosion resistance in 3.5% NaCl, as expected in the absence of an inhibitor.

Among the inhibitors tested, the 3.5% NaCl + modified pectin gel sample shows the highest Rp value (2166 Ω cm^2), correlating to the largest semicircle in a Nyquist plot, suggesting the highest corrosion resistance. This sample also has the highest inhibition efficiency (51.7%), highlighting its superior protective performance against corrosion.

For N-methyldiethanolamine, the polarization resistance was 1415 Ω cm², corresponding to a moderate inhibition efficiency of 26.0%, indicating a reasonable degree of protection against corrosion, though not as effective as modified pectin gel.

Monoisopropyl amine demonstrated a higher polarization resistance of 1965 Ω cm², with an inhibition efficiency of 46.7%, suggesting a substantial increase in corrosion resistance compared to N-methyldiethanolamine. Lastly, monoethanolamine displayed a polarization resistance of 1592 Ω cm², with an inhibition efficiency of 34.2%, reflecting intermediate performance in corrosion protection among the tested amines.

Table 1.8 EIS parameters extracted from the equivalent circuit model

Sample	**Rs (solution resistance) (Ω cm^2)**	**RP (Polarization resistance) (Ω cm^2)**		**CPE (constant phase**	**N**	**Inhibition efficiency (%)**
Bare Carbon Steel in 3.5% NaCl	4.964	1047		$4.3 * 10^{-4}$	0.7974	----------
3.5 NaCl+2g-l pectin	5.089	1072		$1.96 * 10^{-4}$	0.7609	2.3%
3.5% NaCl+2g-l dip pectin	7.9	1541		$5.4 * 10^{-4}$	0.7741	32.0%
3.5% NaCl+ modified pectin gel	28.05	2166		$9.6 * 10^{-4}$	0.5836	51.7%
N-Methyldiethanol Amine	-0.477	1415		$2.9 * 10^{-4}$	0.8786	26.0%
Monoisopropanolamine	13.81	1965		$5.98 * 10^{-4}$	0.6999	46.7%
Monoethanolamine	2.34	1592		$4.5 * 10^{-4}$	0.8282	34.2%

The enhanced polarization resistance in the presence of modified pectin indicates that pectin molecules adsorb onto the steel surface, forming a protective barrier that impedes the charge transfer process associated with corrosion. This is a similar effect that was observed in the amines. This barrier effect not only increases the overall impedance but also modifies the electrochemical environment at the interface, making the corrosion process less favorable.

The Nyquist plot demonstrates the effectiveness of both pectin and amines in enhancing the corrosion resistance of carbon steel in a 3.5% NaCl solution. Pectin, especially in its modified gel form, provides superior protection by forming a robust barrier on the steel surface, significantly increasing the impedance and reducing corrosion. The amines, though not as effective as the modified pectin, also exhibit good corrosion resistance by forming protective films that impede the corrosion process.3.1.3.2 Static corrosion weight loss results

3.1.3.2.1 Static corrosion weight loss results in 1M HCl solution

Table 1.9 Comparison of weight loss of metal coupons after 2 weeks

	Condition	W_1(g)	W_2(g)	W_3(g)	Average	Weight Loss(g)	Corrosion (%)
2 weeks in 1M HCl	Weight before corrosion	3.77704	3.76516	3.79326	3.778487	**0.3348**	**8.862**
	Weight after corrosion	3.48571	3.3929	3.45236	3.443653		
2 weeks in 1M HCl + Pectin	Weight before corrosion	3.80058	3.80363	3.7935	3.799237	**0.084**	**2.221**
	Weight after corrosion	3.74578	3.6806	3.71815	3.714843		
						Inhibitor Efficiency (%)	**74.993**

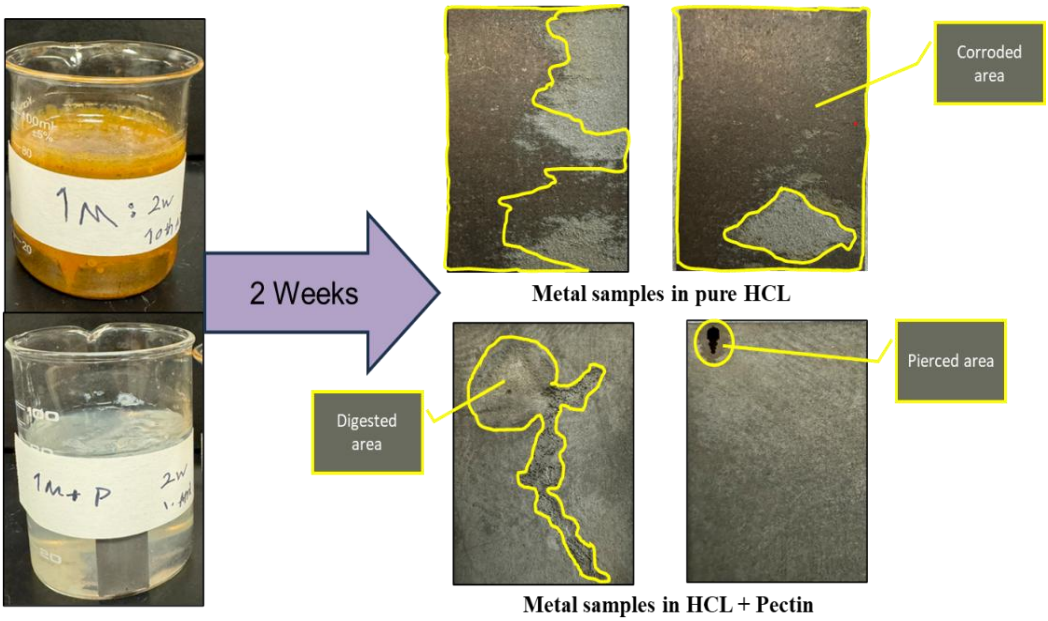

Figure 1.14. Visual Comparison of Metal Coupons Following Two Weeks of Corrosion Tests

Table 1.10 Comparison of weight loss of metal coupons after 4 weeks

	Condition	W_1(g)	W_2(g)	W_3(g)	Average	Weight Loss(g)	Corrosion (%)
4 weeks in 1M HCl	Weight before corrosion	3.77715	3.74674	3.77531	3.76454	**0.35407**	**9.405**
	Weight after corrosion	3.3173	3.43603	3.47818	3.410503		
4 weeks in 1M HCl + Pectin	Weight before corrosion	3.79257	3.7804	3.8158	3.796257	**0.17692**	**4.660**
	Weight after corrosion	3.56769	3.62383	3.66649	3.619337		
						Inhibitor Efficiency (%)	**50.451**

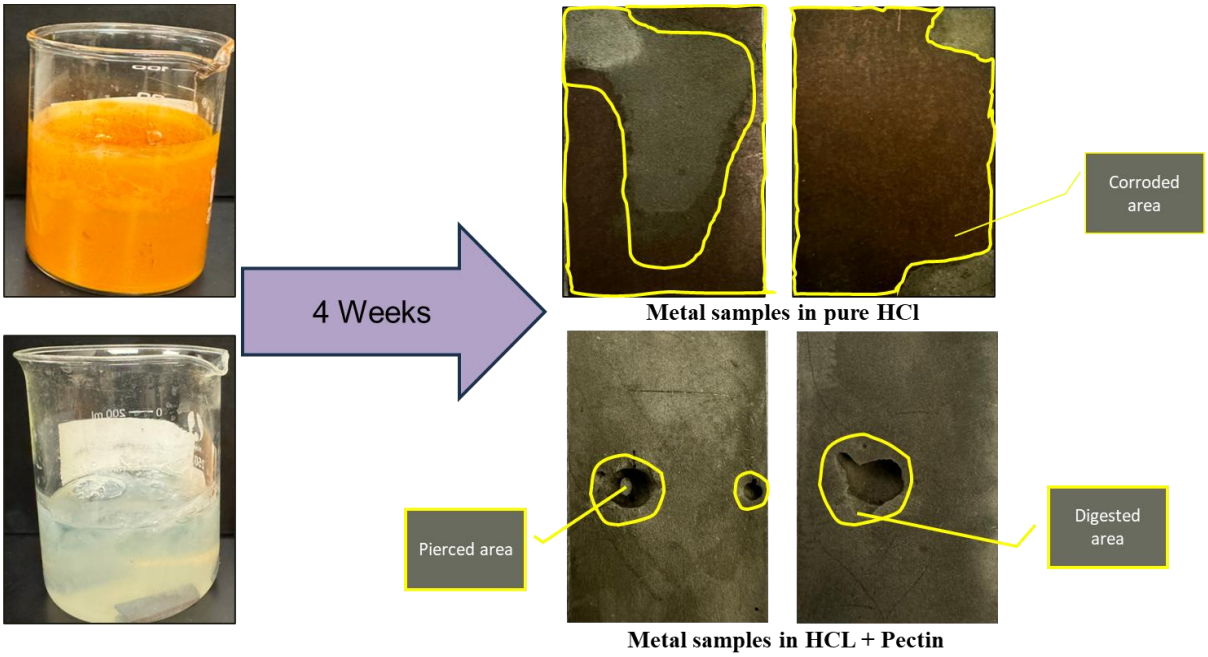

Figure 1.15. Visual Comparison of Metal Coupons Following Four Weeks of Corrosion Tests

Table 1.11 Comparison of weight loss of metal coupons after 6 weeks

	Condition	W_1(g)	W_2(g)	W_3(g)	Average	Weight Loss(g)	Corrosion (%)
6 weeks in 1M HCl	Weight before corrosion	3.7611	3.78515	3.78458	3.776943	**0.46791**	**12.39**
	Weight after corrosion	3.2635	3.29025	3.37335	3.309033		
6 weeks in 1M HCl + Pectin	Weight before corrosion	3.7308	3.7906	3.7784	3.7666	**0.2086**	**5.54**
	Weight after corrosion	3.53846	3.55604	3.57925	3.557917		
						Inhibitor Efficiency (%)	**55.28**

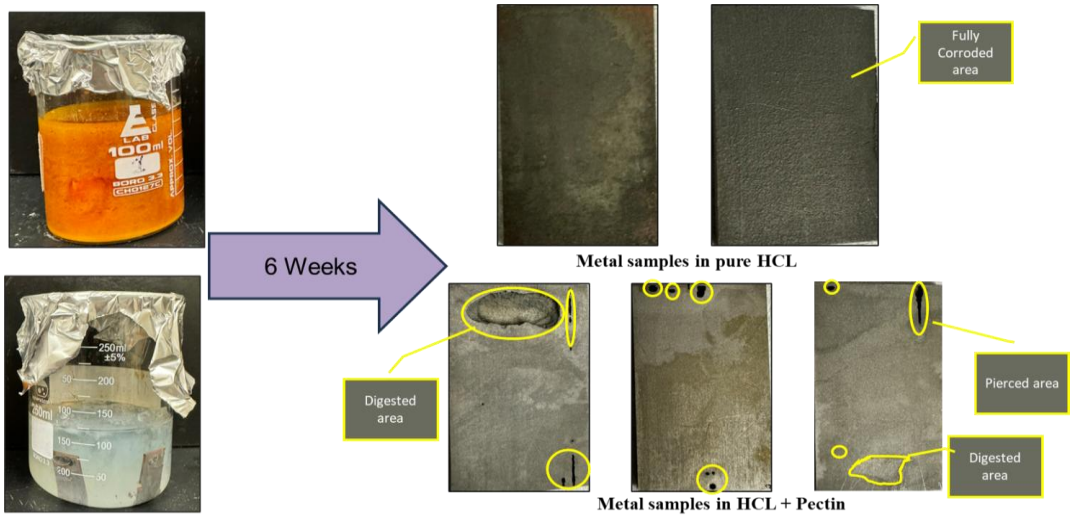

Figure 1.16 Visual Comparison of Metal Coupons Following Six Weeks of Corrosion Tests

Based on the data provided in Tables 1.9, 1.10, and 1.11 and the corresponding figures (1.14, 1.15 and 1.16) in this report, it is evident that pectin has shown significant potential as a green corrosion inhibitor. It effectively reduces metal corrosion in aggressive acidic environments during testing.

In the short-term test spanning two weeks, control samples immersed in 1M HCl exhibited an average corrosion percentage of 8.862% with a weight loss of 0.3348 grams. When pectin was introduced, the corrosion rate significantly dropped to 2.221%, with a weight loss of only 0.084

grams. This translates to an inhibitor efficiency of approximately 74.993%, highlighting pectin's remarkable effectiveness at curbing corrosion in a short period.

Extending the duration to four weeks, the corrosion in control samples slightly increased to a 9.405% corrosion rate and a weight loss of 0.35407 grams. However, samples treated with pectin showed a lower corrosion rate of 4.660% and a weight loss of 0.17692 grams, resulting in an inhibitor efficiency of about 50.445%. Although the effectiveness of pectin decreased compared to the two-week test, it still provided significant protection against corrosion.

For the long-term evaluation over six weeks, the untreated samples showed further increased corrosion, reaching 12.39% with a weight loss of 0.46791 grams. The pectin-treated samples maintained better resistance, showing a corrosion rate of 5.54% and a weight loss of 0.2086 grams, with an efficiency rate of 55.28%. Despite the longer exposure, pectin continued to offer considerable protection, albeit with a slight reduction in efficiency compared to the earlier intervals.

The visual evidence from Figures 1.14, 1.15, and 1.16 corroborates the quantitative data, showing that metal coupons treated with pectin exhibited considerably less surface corrosion than those left unprotected. This consistent trend across all test durations underscores pectin's capability to protect metal surfaces under varied conditions. However, despite the overall reduction in surface corrosion, some samples treated with pectin showed localized damage, such as piercing or the formation of ditches on the metal surfaces. This occurrence, while reducing the general corrosion rate, poses a significant risk if such a phenomenon were to occur in actual pipeline applications, where even minor structural failures can lead to severe consequences.

The occurrence of pitting corrosion is likely attributed to the presence of chloride in the testing medium. Typically, chloride can induce pitting corrosion when the metal surface undergoes passivation, as seen in this test that included an additional corrosion inhibitor. The chloride has the potential to integrate into the protective film formed by the inhibitor and compromise the metal surface at points where the film is weak [1].

In summary, while pectin has demonstrated its effectiveness as a corrosion inhibitor, particularly in the initial exposure stages, its performance shows a slight decline over time but still provides substantial protection compared to unprotected samples. These findings suggest that

pectin holds promise as a sustainable alternative to traditional corrosion inhibitors, especially in scenarios where minimizing environmental impact is crucial. The next phase of research should focus on addressing the observed localized damage to ensure the reliability and safety of pectin as a corrosion inhibitor in real-world applications.

The use of 1M HCl, a highly concentrated acid, was initially chosen to accelerate corrosion for rapid testing outcomes. However, following the recommendations of industry experts, the weight loss tests were also conducted using a diluted 0.25M HCl solution to more accurately simulate the milder corrosive environments typically found in pipelines. Following the established procedure, these tests involved immersing metal coupons in both types of acidic media for six weeks to assess and compare the effects of different acid concentrations on corrosion rates. Table 1.12 shows the average result of the weight loss test on each medium and the efficiency of pectin's corrosion inhabitation compared to the control sample.

Table 1.12 Comparison of weight loss of metal coupons after 6 weeks in diluted corrosive media

	Condition	W_1(g)	W_2(g)	W_3(g)	Average	Weight Loss(g)	Corrosion (%)
6 weeks in 0.25M HCl	Weight before corrosion	3.78612	3.77865	3.79825	3.787673	**1.498**	**39.566**
	Weight after corrosion	2.29125	2.38876	2.18711	2.28904		
6 weeks in 0.25M HCl + Pectin	Weight before corrosion	3.8106	3.7564	3.81138	3.792793	**0.37686**	**9.936**
	Weight after corrosion	3.51761	3.3682	3.36199	3.41593		
						Inhibitor Efficiency (%)	**74.887**

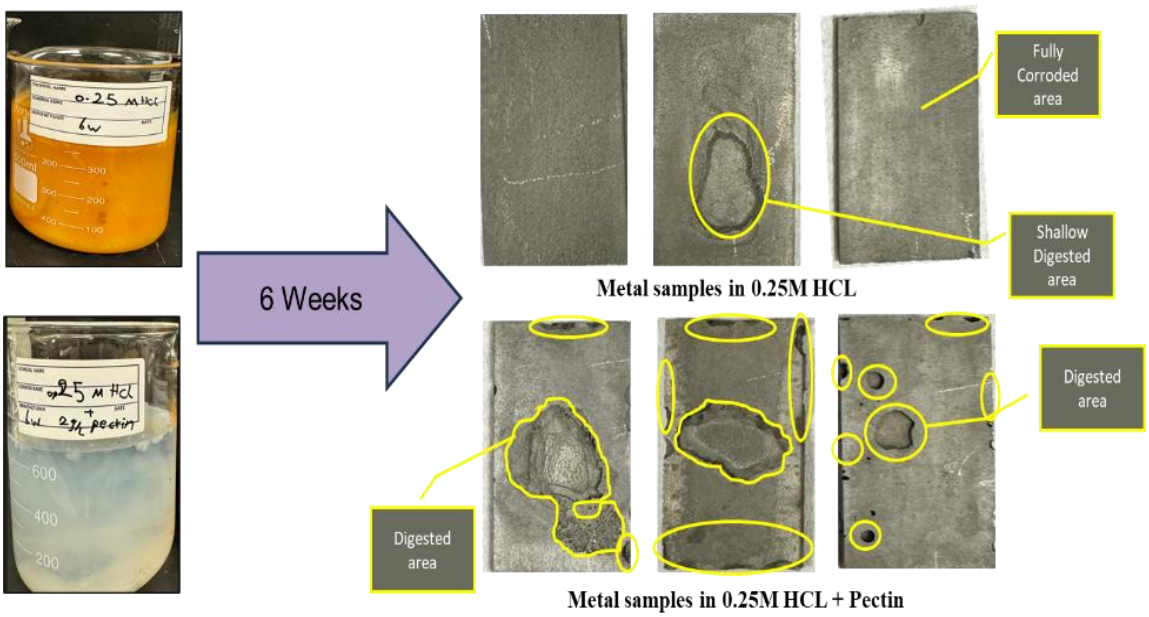

Figure 1.17. Visual Comparison of Metal Coupons Following Six Weeks of Corrosion Tests in 0.25M HCl Solution

The results from the diluted 0.25M HCl tests reveal a significant level of corrosion in the absence of pectin. Initially, the average weight of the metal coupons was approximately 3.787673 grams, which decreased sharply to 2.28904 grams after exposure, resulting in a high corrosion percentage of 39.566%. This level of corrosion underscores the aggressive nature of even diluted acidic environments and emphasizes the necessity for effective corrosion mitigation strategies. It was observed that an increased concentration of chloride accelerates the onset of pitting. However, the impact of chloride concentration on corrosion weight loss remains uncertain, given the various corrosion mechanisms involved [2]. Further investigations are needed to elucidate the corrosion mechanisms at various chloride concentrations.

Conversely, the addition of pectin to the diluted acid solution markedly improved the corrosion resistance of the metal coupons. With pectin, the initial average weight was slightly higher at 3.792793 grams, and the weight after the six weeks was reduced to only 3.41593 grams. This corresponds to a significantly lower corrosion percentage of 9.936%, demonstrating pectin's effectiveness in reducing material loss under corrosive conditions. The calculated inhibitor efficiency of 74.887% highlights the substantial protective capabilities of pectin against corrosion.

Figure 1.17 visually corroborates the quantitative data, showing that metal coupons treated with pectin exhibited considerably less surface damage compared to those immersed in the acid

solution without any protective agent. The metal surfaces in the pectin-treated group showed fewer and less severe signs of surface corrosion, validating the effectiveness of pectin as a corrosion inhibitor. However, even in the diluted medium, occurrences of pierced and extensively corroded spots were observed on metals treated with pectin, which raises concerns about the potential detrimental effects of pectin, particularly its role in creating localized areas of significant damage.

In summary, while the tests in diluted corrosive media highlight the severe impact of even mild acidic conditions on metals, they also demonstrate the notable protective effects of pectin. These results support the potential of pectin as an effective and environmentally friendly corrosion inhibitor for industrial applications, particularly under conditions that mimic real-world corrosive environments. The overall consistency of pectin's protective performance across various conditions points to its appropriateness for broader industrial use. Nonetheless, the observed localized damage necessitates further investigation into pectin's long-term stability and mechanisms to prevent such detrimental effects, ensuring its reliability and safety in practical applications.

3.1.3.2.2 Comparison of corrosion weight loss of A36 and API 5L in 3.5% NaCl solution

We compared the corrosion behavior of A36 and API 5L steel coupons to assess the suitability of A36 for corrosion tests typically conducted with API 5L steel, which is commonly used in gas pipelines. To evaluate the corrosion resistance of these two types of carbon steel in saline environments, we designed an experimental setup in which the steel coupons were submerged in a 3.5% NaCl solution. The tests were conducted at 25°C without any corrosion inhibitors to simulate standard seawater conditions. Our objective was to compare their corrosion behaviors based on weight loss per unit surface area over two weeks. The results of this comparison are summarized in Table 1.13:

Table 1.13. Comparison of corrosion between API 5L and A36 carbon steels

Time	Steel	Surface area	Measured weight	Average	Weight Loss (g)	Corrosion (%)
2W	A36	1 sq. in	Weight before corrosion	3.757553	0.01458	-0.388%
			Weight after corrosion	3.742973		
2W	API 5L	0.5 sq. in	Weight before corrosion	4.99369	0.01037	-0.207%
			Weight after corrosion	4.98332		

The data indicates that both A36 and API 5L steels exhibit similar corrosion behaviors when normalized for surface area. A36 steel showed a corrosion rate of -0.388%, while API 5L steel demonstrated a corrosion rate of -0.207%. It should be noted that the API 5L (e.g., X52 and X70) materials are usually in the form of pipes and cannot be directly used for material corrosion testing. Manufacturing material coupons using raw pipes for screening is very expensive and time consuming due to the large number of samples required. Thus, it is usually common practice that 1080 steel or A36 steel in the form of thin sheet are used for screening of material corrosion testing. Once screening is done, validation testing will be done using API 5L steel samples manufacturing from the raw pipes. The limited experiments shown above indicates that A36 carbon steel has similar corrosion performance compared to that of API 5L under the investigated conditions similar to brine water exposure.

However, to fully confirm that A36 can effectively represent API 5L, further corrosion testing with various corrosion inhibitor candidates is necessary. This will help determine if the differences between the two steel types influence the performance of the corrosion inhibitors, particularly considering the impact of surface conditions. Future tests will focus on comparing the effectiveness of bio-inhibitors on both API 5L and A36 steel to ensure a comprehensive assessment.

3.1.3.2.3 Static corrosion weight loss results in 3.5% NaCl solution

The corrosion tests were conducted using A36 steel sheets that featured a mill (unpolished) finish, were hot-rolled, and conformed to ASTM A36 standards. The sheets, with a thickness of 0.06 inches, were precisely cut into test coupons measuring 2.0 cm by 1.0 cm using a CNC cutter. To simulate moderate corrosion conditions typically found in certain industrial environments, a

3.5% NaCl solution was prepared. Several distinct media were evaluated to assess the corrosion resistance of the steel coupons under varied conditions using benchmark amines and pectin formulations. Following removal from the test media, the coupons were brushed, cleaned with acetone to remove any deposited layers, rinsed with deionized water, and weighed to determine the post-corrosion mass.

Control Group (3.5% NaCl solution)

Table 1.14 Weight loss of control metal coupons after 2,4- and 6 weeks exposure to brine water

Time Interval	Initial Weight (g)	Final Weight (g)	Weight Loss (g)	Corrosion Rate (%)
2 Weeks	3.757553	3.742973	0.01458	-0.388
4 Weeks	3.743287	3.723697	0.01959	-0.523
6 Weeks	3.775787	3.734747	0.04104	-1.087

Table 1.14 presents data for the control sample, which was subjected to a 3.5% NaCl solution (salt water) without the addition of any corrosion inhibitor. The measured weight of the sample is recorded before and after corrosion for three different time intervals: 2 weeks (2W), 4 weeks (4W), and 6 weeks (6W). The weight loss in grams and corresponding corrosion percentage are also noted.

The weight loss progressively increases over time, from 0.01458 g at 2 weeks to 0.04104 g at 6 weeks. Correspondingly, the corrosion rate also shows a worsening trend, increasing from -0.388% at 2 weeks to -1.087% at 6 weeks. This demonstrates that, in the absence of an inhibitor, the sample experiences accelerated corrosion as exposure to the saline solution increases over time.

Figure 1.18. Corroded control samples after 6 weeks

Pectin in Solution

Table 1.15 Weight loss of A36 coupons in solution pectin after 2,4- and 6 weeks of exposure to brine water

Time Interval	**Initial Weight (g)**	**Final Weight (g)**	**Weight Loss (g)**	**Corrosion Rate (%)**	**Inhibition Efficiency (%)**
2 Weeks	3.802147	3.797417	0.00473	-0.124	67.94
4 Weeks	3.799477	3.788150	0.011327	-0.298	43.04
6 Weeks	3.800303	3.771483	0.02882	-0.758	30.23

Table 1.15 presents data on the performance of pectin as a corrosion inhibitor in a 3.5% NaCl solution. The measurements are taken at three different time intervals: 2 weeks (2W), 4 weeks (4W), and 6 weeks (6W). For each interval, the initial and final weight of the sample are recorded, along with the calculated weight loss in grams, corrosion percentage, and inhibition efficiency

The results show that pectin provides some level of corrosion inhibition, but its efficiency decreases over time. The weight loss increases from 0.00473 g in 2 weeks to 0.02882 g in 6 weeks. Correspondingly, the corrosion percentage worsens from -0.124% at 2 weeks to -0.758% at 6 weeks. The inhibition efficiency also drops significantly from 67.94% at 2 weeks to 30.23% at 6 weeks. These results suggest that pectin's ability to inhibit corrosion decreases as the exposure time to the corrosive environment increases.

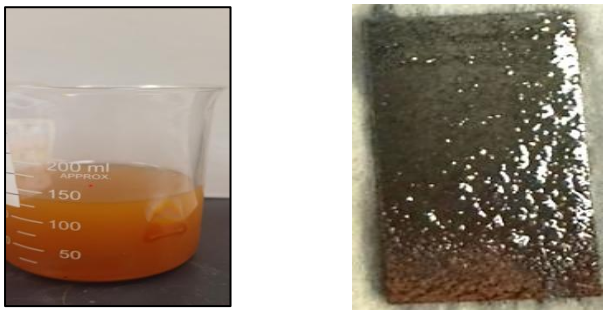

Figure 1.19. Corroded samples after 6 weeks of immersion in pectin solution

Pectin by Dip-Coating

Table 1.16 Weight loss of A36 coupons with dipping in pectin after 2,4 and 6 weeks of exposure to brine water

Time Interval	**Initial Weight (g)**	**Final Weight (g)**	**Weight Loss (g)**	**Corrosion Rate (%)**	**Inhibition Efficiency (%)**

2 Weeks	3.790293	3.781813	0.00848	-0.224	42.34
4 Weeks	3.768933	3.753663	0.01527	-0.405	22.58
6 Weeks	3.794737	3.761410	0.03333	-0.878	19.20

Figure 1.20. Corroded samples with a pectin film by dip-coating after 6 weeks

Table 1.16 presents corrosion data for a sample dipped in pectin solution as an inhibitor in a 3.5% NaCl environment over 2, 4, and 6 weeks. At 2 weeks, the weight loss was 0.00848 g with a corrosion rate of -0.224% and inhibition efficiency of 42.34%, indicating moderate protection. At 4 weeks, weight loss increased to 0.01527 g, corrosion rose to -0.405%, and inhibition efficiency dropped to 22.58%, showing a significant reduction in protection. By 6 weeks, weight loss further rose to 0.03333 g, corrosion worsened to -0.878%, and inhibition efficiency fell to 19.20%, indicating minimal long-term protection.

Monoisopropanolamine by Dip-Coating

Table 1.17 Weight loss of A36 coupons protected with dipping in Monoisopropanolamine after 2, 4 and 6 weeks of exposure to brine water

Time Interval	**Initial Weight (g)**	**Final Weight (g)**	**Weight Loss (g)**	**Corrosion Rate (%)**	**Inhibition Efficiency (%)**
2 Weeks	3.786803	3.782583	0.00422	-0.111	71.28
4 Weeks	3.801693	3.792720	0.008972	-0.236	54.90
6 Weeks	3.760920	3.742096	0.018823	-0.500	53.95

The above table presents corrosion data for a sample in a 3.5% NaCl environment using monoisopropanolamine (an amine) as a corrosion inhibitor over 2, 4, and 6 weeks. At 2 weeks, the weight loss was 0.00422 g, with a corrosion rate of -0.111% and an inhibition efficiency of 71.28%, indicating strong initial protection. At 4 weeks, the weight loss increased to 0.00897 g,

with the corrosion rate rising to -0.236% and inhibition efficiency dropping to 54.90%, showing a reduction in protective performance. By 6 weeks, the weight loss further increased to 0. 01882 g, with a corrosion rate of -0.500% and inhibition efficiency at 53.95%, indicating that the inhibitor's effectiveness stabilizes but still provides moderate long-term protection.

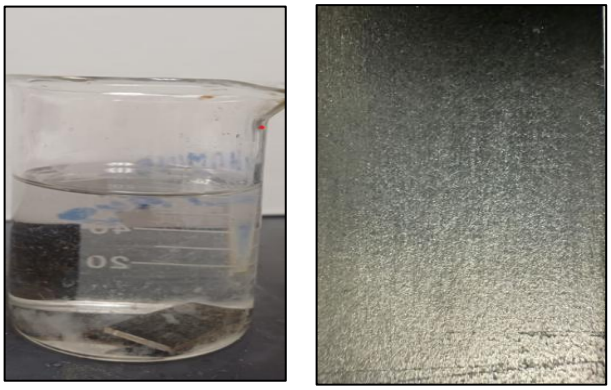

Figure 1.21 Corroded samples with a monoisopropanolamine film by dip-coating after 6 weeks

NMDEA (N-methyldiethanolamine) by Dip-Coating

Table 1.18 Weight loss of A36 coupons protected with dipping in N-methyldiethanolamine after 2,4 and 6 weeks of exposure to brine water

Time Interval	**Initial Weight (g)**	**Final Weight (g)**	**Weight Loss (g)**	**Corrosion Rate (%)**	**Inhibition Efficiency (%)**
2 Weeks	3.792447	3.790247	0.0022	-0.058	85.05
4 Weeks	3.804887	3.799700	0.005187	-0.136	73.95
6 Weeks	3.769143	3.754210	0.014933	-0.396	63.55

The above table presents corrosion data for a sample in a 3.5% NaCl environment using N-methyl diethanolamine (NMDEA) as a corrosion inhibitor over 2, 4, and 6 weeks. At 2 weeks, the weight loss was 0.0022 g, with a corrosion rate of -0.058% and an inhibition efficiency of 85.05%, indicating excellent initial protection. At 4 weeks, the weight loss increased to 0.00519 g, with the corrosion rate rising to -0.136% and inhibition efficiency dropping to 73.95%, reflecting a decline in protective performance over time. By 6 weeks, the weight loss further increased to 0.01493 g, with the corrosion rate reaching -0.396% and inhibition efficiency reducing to 63.55%, suggesting that while the inhibitor still provides protection, its effectiveness diminishes as the exposure time lengths.

Figure 1.22. Corroded samples with a NMDEA film by dip-coating after 6 weeks

Monoethanolamine by Dip-Coating

Table 1.19. Weight loss of metal coupons protected with dipping in Monoethanolamine after 2,4 and 6 weeks of exposure to brine water

Time Interval	**Initial Weight (g)**	**Final Weight (g)**	**Weight Loss (g)**	**Corrosion Rate (%)**	**Inhibition Efficiency (%)**
2 Weeks	3.777270	3.759493	0.017777	-0.471	-21.29
4 Weeks	3.779160	3.756353	0.022807	-0.603	-15.31
6 Weeks	3.794317	3.759777	0.034540	-0.910	16.25

Table 1.19 presents corrosion data for a sample in a 3.5% NaCl environment using monoethanolamine as a corrosion inhibitor over 2, 4, and 6 weeks. This amine demonstrates poor performance as an inhibitor, with negative inhibition efficiencies in the early stages. At 2 weeks, the weight loss was 0.01778 g, with a corrosion rate of -0.471% and a negative inhibition efficiency of -21.29%. This indicates that instead of reducing corrosion, the inhibitor worsened the corrosion rate compared to the control. At 4 weeks, the weight loss increased to 0.02281 g, with a corrosion rate of -0.603% and the inhibition efficiency remained negative at -15.31%, reflecting continued poor performance. At 6 weeks, while the weight loss further increased to 0.03454 g and the corrosion rate worsened to -0.910%, the inhibition efficiency improved slightly to 16.25%. However, despite this small improvement, monoethanolamine remains the worst-performing amine overall, with mostly negative inhibition efficiencies indicating an acceleration of corrosion.

Figure 1.23. Corroded samples with a monoethanolamine film by dip-coating after 6 weeks

The following table summarizes the average efficiency of various inhibitors tested in a 3.5% NaCl environment. N-methyldiethanolamine exhibits the highest average efficiency at 74.18%, followed by monoiso-propanolamine at 60.04%, both demonstrating strong inhibition properties. Pectin in solution (47.07%) and dip-coated pectin (28.04%) show moderate inhibition capabilities, though they are less effective than the amines. Conversely, monoethanolamine has the poorest performance with a negative efficiency of -6.78%, indicating it accelerates corrosion rather than preventing it. The data indicates that the tested bio-inhibitor was less effective than traditional chemical inhibitors, particularly N-methyldiethanolamine.

Table 1.20. Comparison of the average efficiency of inhibitors

Inhibitors	**The average efficiency of inhibitors**
Pectin in solution	47.07%
Pectin by dip-coating	28.04%
Monoisopropanolamine by dip-coating	60.04%
Nmethyldiethanolamine by dip-coating	74.18%
Monoethanolamine by dip-coating	-6.78%

3.2 Task 2: Simulation-based inhibitor optimization in Gas Gathering and Transportation Pipelines

3.2.1 Task 2.1: Numerical simulation of multiphase flow for inhibitor distribution in gas pipeline systems

We have employed CFD methods to model the dynamics of multiphase flow within gas pipelines, which serves as the benchmark results for the future AI-augmented computing framework. This includes simulating the flow of natural gas and solid inhibitor particles under various operational scenarios to mimic real-world pipeline conditions. A key aim of this subtask is to evaluate the efficiency of corrosion inhibitors in different pipeline environments. The study analyzed how varying flow rates, pressures, temperatures, and pipeline geometries influence the performance and distribution of these inhibitors. It should be noted that there are existing CFD studies for pipeline flow simulation, and our objective and focus is on the development and verification of AI-augmented computing for efficient and accurate simulation.

Flow-induced corrosion is primarily attributed to the fluid dynamics within the pipeline, where multiple phases containing gases and occasionally solid inhibitor particles - interact with the inner walls. This interaction often results in the disintegration of the protective inhibitor layer, leaving the metal surface vulnerable to corrosive agents. Erosion-corrosion, on the other hand, is a more complex form, where the mechanical action of moving fluids and particles exacerbates the corrosion process.

Understanding the distribution and behavior of these different phases within the pipeline system is crucial for a comprehensive evaluation of corrosion risk. The presence and dynamics of each phase—be it gaseous (natural gas, corrosive gases like CO2 and H2S) or solid (inhibitor particles)—can significantly influence the rate and severity of pipeline corrosion.

In this subtask, we assessed the efficacy of corrosion inhibitors in such complex environments using advanced Computational Fluid Dynamics (CFD) simulations. Corrosion inhibitors are chemicals introduced into the pipeline to form a protective film on the metal surface, thus mitigating the corrosive impact of the internal environment. However, the performance of these inhibitors is not solely dependent on their chemical properties; it is also significantly influenced by the flow dynamics within the pipeline, which is a function of the flow dynamics of the multi-phase system.

Our CFD simulations emphasized the transportation conditions of natural gas pipelines, taking into account the multiphase nature of the internal flow. By varying parameters such as the volume fractions of different phases, flow velocities, pressures, and temperatures, alongside considering different pipeline geometries, we strived to create a comprehensive picture of the conditions under which inhibitors operate. These simulations are designed to offer insights into how efficiently inhibitors can protect various sections of the pipeline under a range of operational scenarios.

In tackling the complexities of multiphase flow in natural gas pipelines, the application of CFD models is indispensable. CFD theory employs computational power to resolve the partial differential equations governing fluid flow. This approach facilitates a deeper understanding of fluid dynamics by analyzing flow fields and other physical characteristics. The ANSYS software is employed for physical modeling and mesh generation in pipeline systems. A structured grid was chosen due to its ability to deliver high-quality solutions with smaller cells. Figure 2.1 provides an example of a 3D straight pipeline mesh.

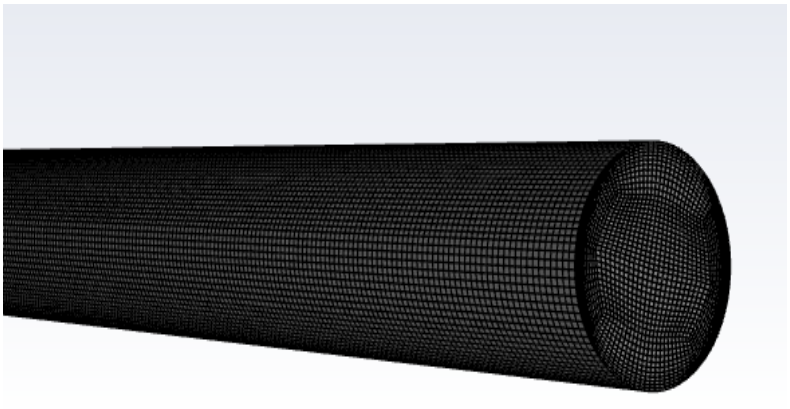

Figure 2.1. Example of the pipeline mesh

In our comprehensive analysis of the multiphase system within gas pipelines, a variety of parameters are meticulously considered to ensure a thorough understanding of the dynamics at play. These parameters are categorized into three primary groups: Pipeline Properties, Flow Properties, and Operational Conditions.

- **Pipeline properties**

o Geometry: The shape, size, and layout of the pipeline, including length, diameter, and the presence of bends or junctions, which influence flow dynamics and potential corrosion sites.

o Material: The type of material used for pipeline construction, such as steel or composite materials, which determines its resistance to corrosion and mechanical stress.

o Roughness: The internal surface texture of the pipeline, affecting flow turbulence and the adherence of inhibitor films.

- **Flow Properties:**

o Gas: The properties of the natural gas being transported, including its composition, density, and viscosity.

o Inhibitor: The chemical properties of the corrosion inhibitor, its interaction with other phases, and its efficacy in different conditions.

o Corrosive gases: The concentration and behavior of corrosive gases like CO2 and H2S, which significantly contribute to pipeline corrosion.

o Sloid particles: The characteristics of solid particles such as sulfur, including their size, concentration, and abrasive qualities.

- **Operational Conditions:**

o Pressure: The operational pressure within the pipeline, which influences the behavior of gas and solid phases and the effectiveness of the inhibitor.

o Temperature: The temperature inside the pipeline, affecting fluid properties, chemical reactions, and the performance of the corrosion inhibitor.

o Flow rate: The velocity of the flow within the pipeline, which impacts shear stress, erosion potential, and inhibitor distribution.

o Inhibitor injection rate: The rate at which the corrosion inhibitor is introduced into the pipeline, crucial for maintaining optimal protection.

o Inhibitor thickness: The thickness of the inhibitor layer on the pipeline's interior, a factor critical to its protective ability.

o Inhibitor concentration: The concentration of the inhibitor in the pipeline, affecting its ability to prevent corrosion.

In this study, we address a fluid dynamic system characterized by incompressible and Newtonian fluid properties. The behavior of such a fluid is governed by the Navier-Stokes equations, which are fundamental to fluid mechanics. These equations are presented as follows:

$$\tilde{\mathrm{N}} \times u = 0 \tag{5}$$

$$\mathrm{r}\left(u\frac{\partial u}{\partial t} + u \times \tilde{\mathrm{N}}u\right) = -\tilde{\mathrm{N}}p + m\tilde{\mathrm{N}}^2\mathrm{u} \tag{6}$$

To effectively resolve the Navier-Stokes equations within the realm of Computational Fluid Dynamics (CFD), a variety of numerical methods are available. These include the finite difference method, finite element method (FEM), boundary element method, finite volume method, and finite analysis method. Among these, the FEM is particularly noteworthy for its high accuracy and adeptness in managing complex boundary conditions.

The application of FEM is bolstered by the use of sophisticated software platforms such as ABAQUS, ANSYS, and MSC. ANSYS, in particular, stands out due to its comprehensive and flexible suite of modules that are well-suited to a wide range of engineering applications. Within the scope of gas-inhibitor two-phase flow analysis using ANSYS, the careful selection of specific models, particularly those for turbulence and multiphase flow, is vital.

The realm of turbulence modeling has seen extensive research, revealing distinct advantages for various models. The realizable k-ε equation, for instance, is favored for its optimal blend of computational efficiency and accuracy, proving especially effective in scenarios involving rotating and separation flows. In terms of multiphase flow analysis, ANSYS offers several model options, such as the Volume of Fluid (VOF), Euler, and mixture models. The VOF model, in particular, is highly proficient at tracking interface separation phenomena in gas-inhibitor two-phase flows, a conclusion well-supported by existing literature.

1) Straight Pipeline Simulation

The flow dynamics of a gas-inhibitor mixture within pipeline systems exhibit considerable variation under different operational conditions. This phenomenon is illustrated in the preliminary 2D flow simulation depicted in Figure 2.2. Here, the pipeline's flow field is represented as a three-phase amalgamation of gas and the corrosion inhibitor, with the latter being introduced from the pipeline's top. A notable observation from the simulation is the tendency of the inhibitor to initially align along the pipeline's upper section before gradually descending towards the bottom, influenced by gravity. Over time, a decrease in the inhibitor's concentration at the top is observed, consequently heightening the risk of top-of-line (TOL) corrosion.

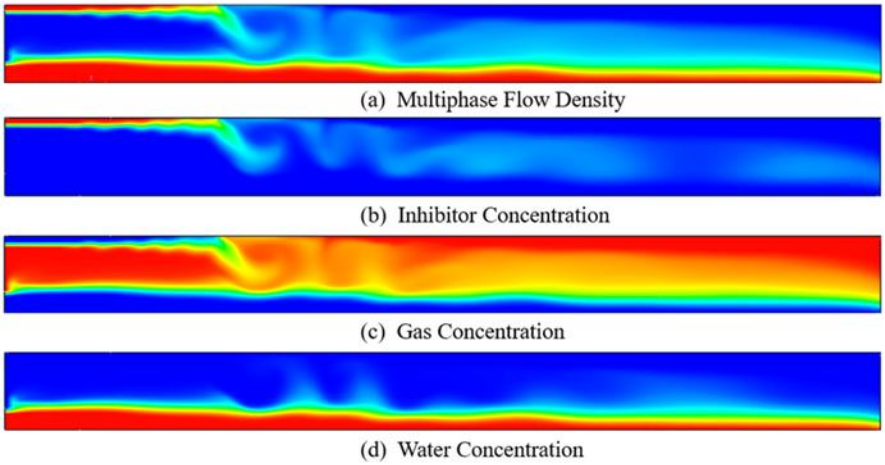

Figure 2.2. Illustration of the numerical simulation depicting corrosion inhibitor distribution. (Brighter areas represent higher concentrations or densities.)

The simulation also sheds light on how varying the flow rate impacts the inhibitor's behavior. An increase in the flow rate appears to decelerate the inhibitor's downward movement, thus offering enhanced protection to the pipeline's upper wall. Concurrently, an escalation in gas flow and turbulence is observed to diminish the gas concentration, effectively mitigating the risk of bottom-of-line (BOL) corrosion. Therefore, the simulation suggests that elevating both the gas flow rate and turbulence could serve as a strategic measure to safeguard both the upper and lower sections of the pipeline against corrosion.

Building upon these insights, the proposed study aims to develop advanced 3D simulation models. These high-fidelity models are intended to provide a more detailed and nuanced understanding of the complex interactions within the gas-inhibitor system under varying operational scenarios, thereby enabling more effective corrosion prevention strategies in pipeline systems.

2) Inclined Pipeline Simulation

Prior simulation research has provided key insights into the factors influencing the distribution of corrosion inhibitors in pipeline systems. Critical variables such as gas flow rate, filling rate, pipe inclination, and the size of particles have been identified as major contributors to how corrosion inhibitors are dispersed within pipelines. The complexity of pipeline geometry, particularly in gathering pipelines and certain segments of transportation pipelines, plays a pivotal role in altering the distribution and efficacy of these inhibitors.

A striking example of this is illustrated in the preliminary study showcased in Figure 2.3. This study highlights the significant effect of even a slight inclination, denoted as angle θ, on the

distribution of the three-phase flow - consisting of gas and inhibitors - within pipeline systems. Such inclinations are a common feature in gathering pipeline systems and serve as a testament to the nuanced impact of pipeline geometry on flow dynamics. This understanding underscores the need for thorough analysis and tailored strategies in corrosion inhibitor deployment, particularly in pipeline systems with complex geometries or variable operational conditions.

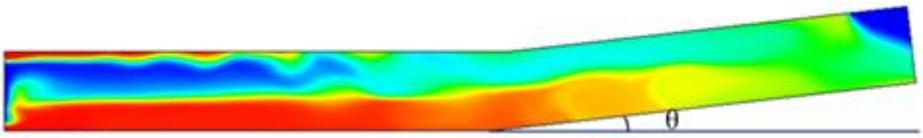

Figure 2.3. Illustration of the numerical simulation depicting corrosion inhibitor distribution in an inclined pipeline.

3) Complex Pipeline Simulation

Figure 2.4 presents a compelling illustration of the complexities in pipeline design and their implications for corrosion control. A notable example is the horseshoe bend in the pipeline, commonly encountered when navigating around obstacles. This specific design feature can lead to the accumulation of gas at the first joint, referred to as location 1, potentially resulting in bottom-of-line (BOL) corrosion. The accumulation of gas at this juncture not only poses a risk to the pipeline's integrity but also disrupts the effective transport of both gas and corrosion inhibitors. Consequently, this leads to an uneven distribution of the inhibitor, particularly evident after the second joint, designated as location 2. In this area, the top section of the pipeline, or the top-of-line part, suffers from a lack of adequate inhibitor protection.

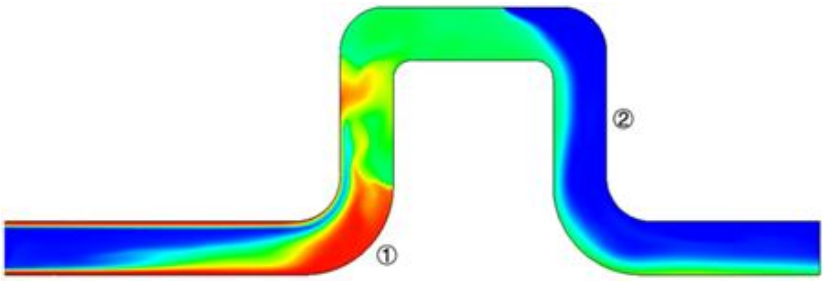

Figure 2.4. Illustration of the numerical simulation depicting corrosion inhibitor distribution in horse-shoe bent pipeline.

Interestingly, the presence of an inclination in the pipeline's design can have a dual effect. On one hand, it contributes to a more uniform distribution of contents within the pipeline, which is beneficial for protecting the upper section of the rear pipe. On the other hand, this same inclination can inadvertently promote the accumulation of gas in the front pipe, thereby elevating the risk of BOL corrosion.

This nuanced interaction between pipeline geometry, fluid dynamics, and corrosion prevention underscores the importance of carefully selecting the parameters for corrosion inhibitors. Such selection is crucial in ensuring effective corrosion prevention, particularly in pipeline systems with complex geometries or varying operational conditions. It highlights the need for a tailored approach in designing and implementing corrosion prevention strategies, taking into account the unique characteristics and challenges of each pipeline system.

3.2.2 Task 2.2: AI-assisted inhibitor implementation optimization in gathering and transportation pipelines

Applying the corrosion inhibitor, the protective film would be in a sustained weakening by the flow and will gradually loss adhesion over time. Therefore, the inhibitor film attached on the pipe wall needs to supplement at certain intervals. However, Characteristics of many new types of inhibitors are not clear, resulting in the difficulty to specify the plan for the utilization of corrosion inhibitors. Overly frequent supplementation of inhibitors will cause unnecessary resource waste. On the contrary, failure to timely fill the failed protective film may lead to irreversible damage to the pipe wall and the reduction in its service life. This research aims to investigate the flow-induced degradation of the inhibitor film.

Flow-induced degradation is primarily attributed to the fluid dynamics within the pipeline, where multiple phases interact with the inner walls. Compared to the static state, this interaction more likely to trigger the disintegration of the protective inhibitor layer, leaving the metal surface vulnerable to corrosive agents. Wall shear stress (WSS) serves as a key metric for assessing the impact of multiphase flow on corrosion inhibitor films. Therefore, the stability of the corrosion inhibitor film under fluid flow is evaluated using WSS as a pivotal reference, highlighting the critical relationship between flow dynamics and the integrity of corrosion protection.

Besides, microscale studies of WSS prediction cannot take into account the global flow field and are required to configure appropriate boundary conditions that are usually given through experience or macroscopic analysis. There is a lack of relevant research in the field of corrosion inhibitor desorption, especially for the new varieties involved in Task 1. Therefore, further macroscopic analysis of the artificially enhanced flow field was performed, laying the foundation for further efficient prediction of the injection and transportation characteristics of corrosion inhibitors.

In this subtask, we have built a network to efficiently predict WSS from roughness profile at microscale, which can contribute to later research of specifying the degradation of corrosion inhibitors in the flow. At macroscale, we developed an efficient surrogate model to temporally predict PDE solutions and enhance the Bayesian optimization methods with adaptive sampling to improve the efficiency and accuracy of uncertainty quantification that reduces the need for high-fidelity data.

3.2.2.1 Prediction of wall shear stress

The wall roughness we used is set at a 0.05m-length boundary of the 2-D pipe with the remaining part of being totally smooth for each computational case of CFD, as shown in Figure 2.5, which ensures the fully developed flow field in the enough length. Specifically, each training or testing set contains the data at 200 continuous points, in which original values of x-coordinate and WSS are used, while the derivative of y over x ($y' = \Delta y / \Delta x$) replace y values to form the dataset. Here, x and y' are set as the input of Fourier neural operator (FNO), and WSS calculated by CFD as the output.

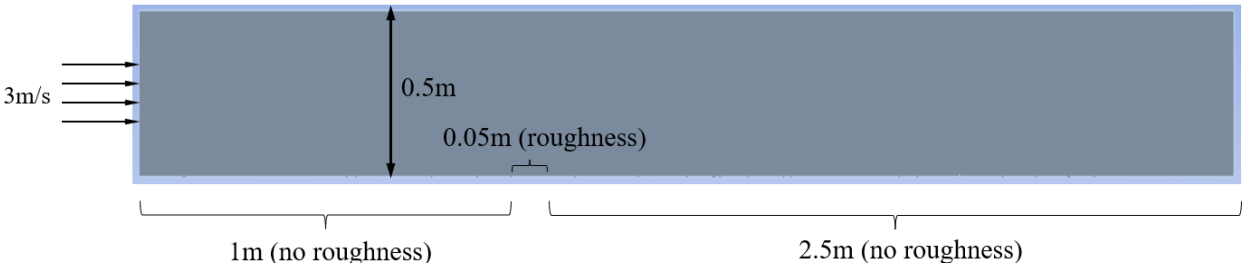

Figure 2.5. 2D pipe with wall roughness.

The comparison testing results with traditional fully-connected network demonstrated better adaptability of FNO in WSS prediction. However, we extracted training and testing data from the same roughness case in the previous work, and the existing FNO model was limited in prediction with the shape of wall roughness that never occur in the training set. For this reason, we aim to improve the existing FNO model to predict WSS with different roughness information.

In this study, roughness profiles are designed in trigonometric functions as $y=a*\cos(f*x)+a$, where a and f denote the factors of amplitude and frequency, respectively. In current research, a is considered in the series [0.12, 0.14, 0.16, 0.18] (millimeter), and f is in [0.05, 0.10, 0.15, 0.20, 0.25]. In total, twenty cases with different combinations of a and f are used. The roughness shapes are integrated into the pipe segment in Ansys Fluent 2023, in which related settings about meshing and solution are similar as before.

CFD results provide the WSS data corresponding to each point of roughness shapes that is still set as the only output of the FNO model. Different from the previous work, y-coordinate is incorporated as the input. As a result, three dimensions of data (x, y and $y'=\Delta y/\Delta x$) are used to characterize location information. Figure. 2.6 illustrates the data extraction approach that cut out continuous points from a case and divides it into the “previous”, “middle” and “next” segments. Location information of these three segments is totally set as the input, while only WSS with

respect to the middle segment is used as the output. This implementation is under the consideration that WSS is affected by near roughness shapes. Besides, the figure also shows that data points in each case are extracted by moving slicing, and the moving step is usually less than the length of the full segments to increase the available data. In our cases, the lengths of the previous, middle and next segments are 200, 50 and 200 points, respectively; The moving step is set as 50 points.

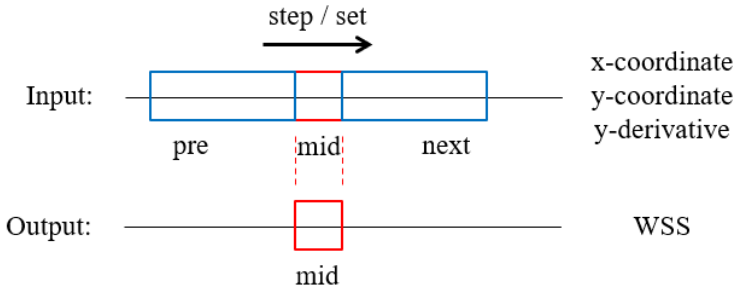

Figure 2.6. Illustration of data extraction.

To illustrate the surrogate model more clearly, Figure 2.7 depicts the framework of the applied FNO model suitable to our cases. Considering one batch of data, the initially input is a matrix with three rows. It would be first expanded to a new one with more rows, which can be regarded as an encoder process incorporating more information. Then, a series of fast Fourier transform (FFT) and inverse fast Fourier transform (IFFT) are applied to the row space. Later, two row linear transfer are performed to condense the data to a row vector. Traditional FNO only got the output with the same size as input. Therefore, we try two types of transfer to adjust the column number: The one is column linear reduction, and another is to directly cut down the redundant points of the “previous” and “next” segments. The comparison shows the latter one is better and is chosen as the final reduction approach. This is reasonable, since FNO attaches importance to the location arrangement of each point. But the column transfer would hurt this arrangement. It can be also seen that in the previous layer transfer, FNO learned the data relationship only from row transfers.

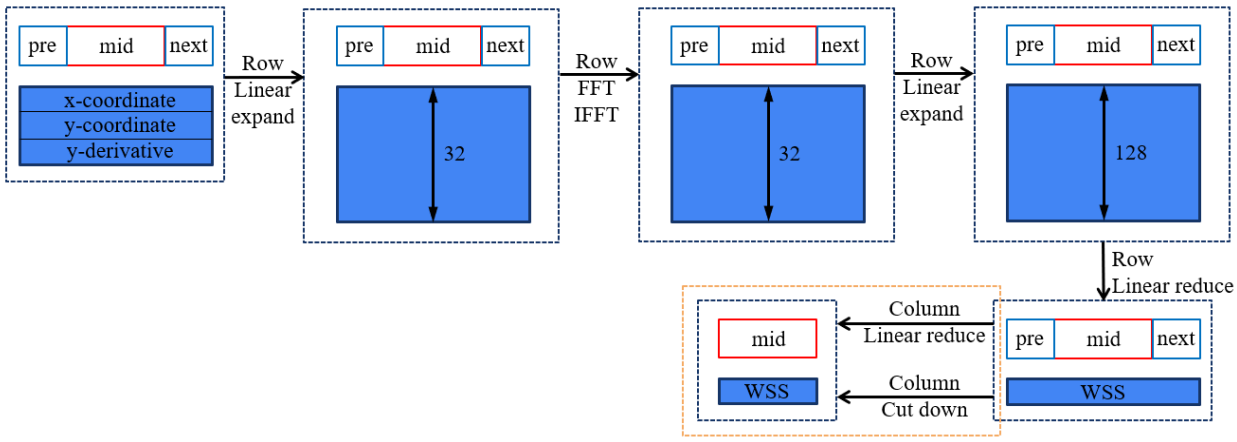

Figure 2.7. Illustration of data flow in FNO.

The roughness case with a=0.1 and f=0.15 are used as the testing set, and the datasets corresponding to the remaining nineteen cases as training sets. Figure 2.8 shows predicted results of WSS from different segments of the testing roughness case. Three different simulation results are shown and each simulation has different surface roughness profiles (randomly generated). Nevertheless, the predicted WSS follows a similar trend of change as true values. Taking into accounts the most unfavorable situations, we were focus on the peak values, which cannot be always accurately predicted. Peak values in the three sets of Figure 2.8, for example, got an obvious difference between target and predicted values. This may mainly due to the uncertainty of the WSS data that the computational WSS from CFD has patent fluctuation. The complexity of the flow lead to this uncertainty even in a regular periodic roughness shape, let alone more chaotic boundary shapes in practice. The uncertainty appeared in WSS prediction should be quantified and will be further discussed later.

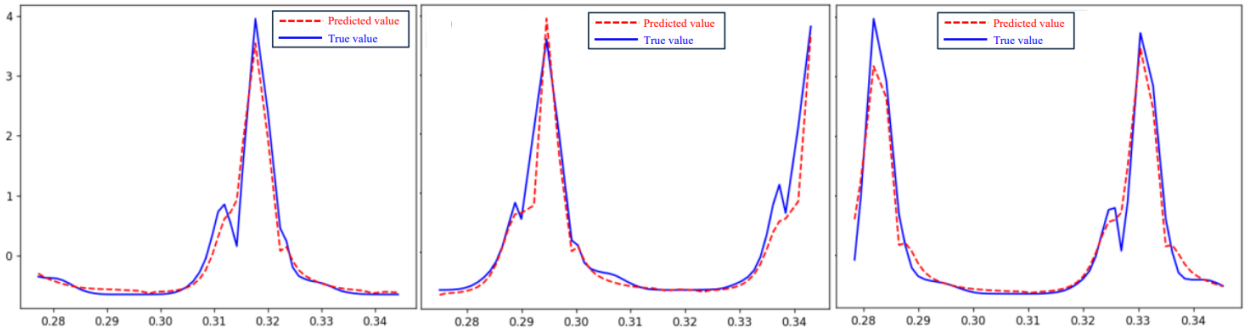

(a) Simulation 1 (b) Simulation 2 (c) Simulation 3

Figure 2.8. Predicted WSS with FNO from sampled segments with different phases.

To investigate the in-depth research about the application of FNO on WSS prediction, two groups of contrastive studies are performed. The first one is under different data normalization approach. Figure 2.9 depicts the prediction results under four contrastive conditions: (a) all datasets conformed to the same mean values and variance, which are calculated from the integrity of the data in nineteen training cases, and this approach is applied by the FNO used in the last section; (b) data of each simulation case is individually normalized; (c) data of each training and testing sample, i.e., cut-out segment, is individually normalized; (d) no normalization is performed. There is a certain difference among the first three conditions. But as mentioned before, this may be due to the uncertainty of computational WSS. In total, the first three normalization approaches are accessible to achieve acceptable prediction results. On the contrary, the result in Figure 2.9(d) shows that non-normalization cannot lead to a good prediction in our case.

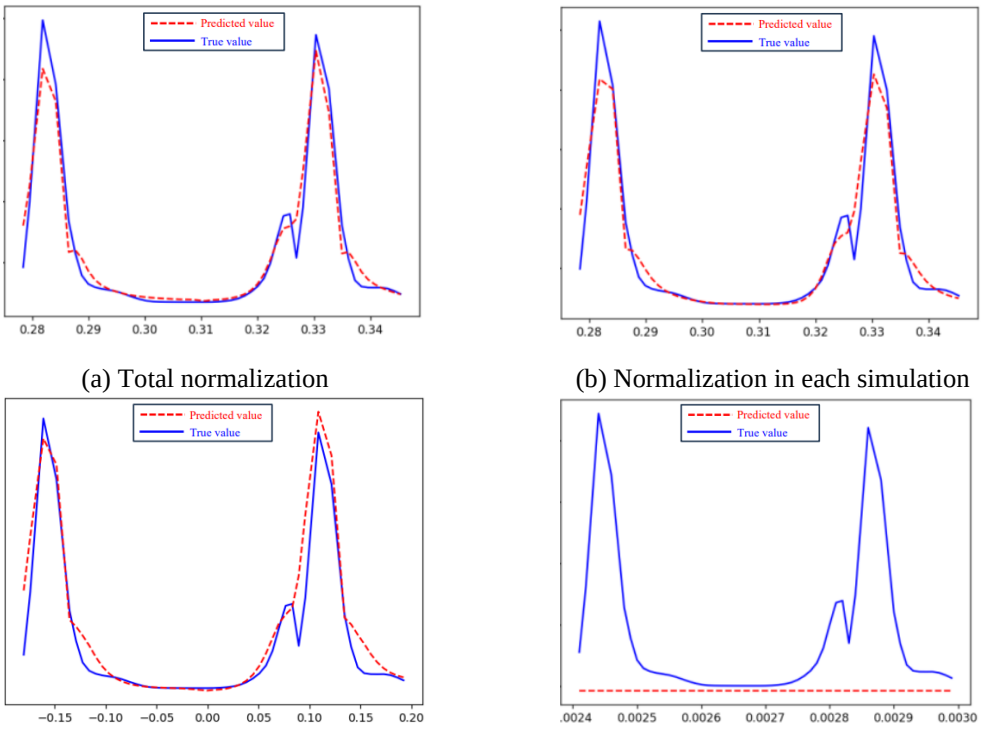

(a) Total normalization

(b) Normalization in each simulation

(c) Normalization in each sample

(d) No normalization

Figure 2.9. Predicted WSS under different conditions of data normalization.

Another contrastive study is applied with the traditional fully-connected neural network (FCNN) with the model shown in Figure 2.10. Except that the FFT and IFFT layers are eliminated, other network setup of this model is same as FNO used in our research. The WSS results predicted by FCNN are shown in Figure 2.11, which are much worse than those in Figure 2.7 (results with FNO). This comparison emphasizes the superiority of FFT-related layers in the FNO framework.

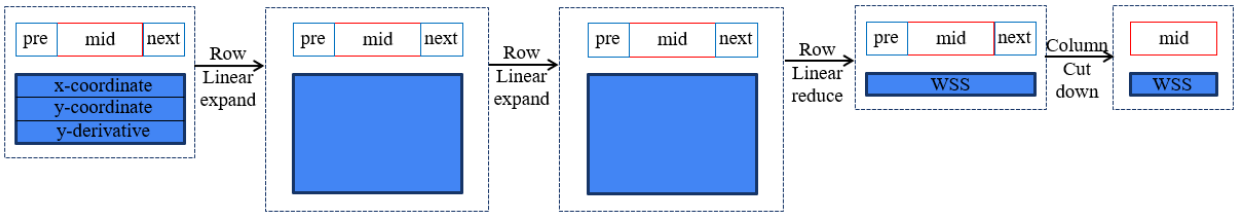

Figure 2.10. Illustration of data flow in FCNN.

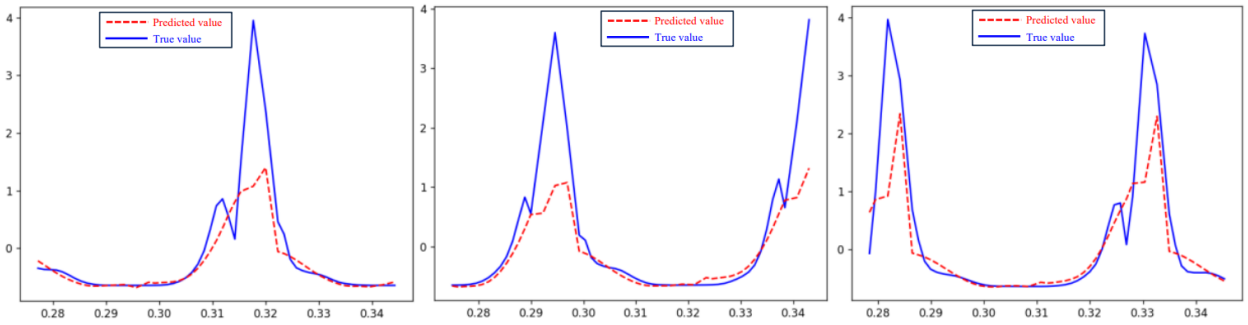

(a) Simulation 1 (b) Simulation 2 (c) Simulation 3

Figure 2.11. Predicted WSS with FCNN from different sampled segments.

As further improvement, we introduced the uncertainty qualification approach into FNO that considers both aleatoric uncertainty (AU) and epistemic uncertainty (EU). In a word, the former is about measurement noise and inadequate accuracy, and the latter is mainly about untouched points in training data. At the stage of implementation, the loss function of FNO containing AU has the following expression:

$$\text{Loss} = \frac{1}{N}\sum_{i=1}^{N}\frac{1}{2}exp(-\sigma)\,\|y_i - f(x_i)\|^2 + \frac{1}{2}\sigma \qquad (7)$$

Where N denotes the number of datasets; y_i and $f(x_i)$ are the target value and the prediction output of the *i*-th dataset, respectively; The variance σ is produced from the full layers, that is, from the input to output. Another network with the same framework but additional sets of parameters are trained for σ. EU can be quantified by adding the dropout into a layer, i.e., randomly dropping some neurons for data transfer.

The prediction results with uncertainty quantification are depicted in Figure 2.12, in which the blue areas show the 95% confidence interval of the prediction values. These results conform to the actual situation, that is, both AU and EU are larger when the actual prediction error is larger, such as those in the peak of WSS. But up to now, there is no specific method to determine to what

extent the uncertainty qualification results can reflect the real uncertainty. It still asked for more tests and clarity.

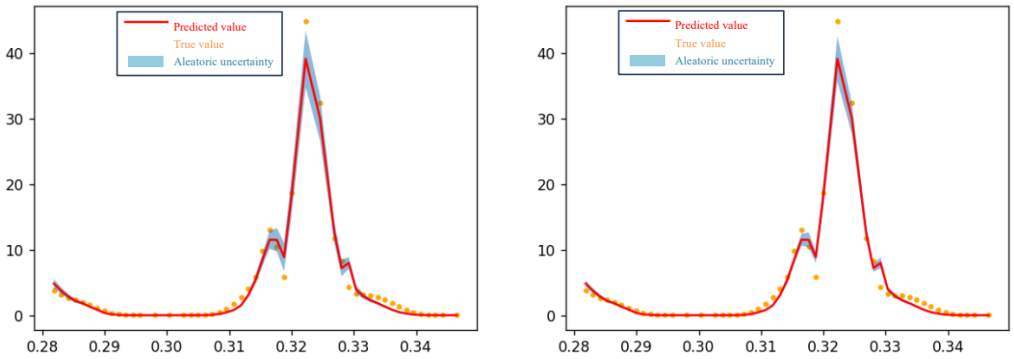

(a) Aleatoric uncertainty (b) Epistemic uncertainty

Figure 2.12. Quantification results of WSS with FNO in the same simulation.

With given WSS, an inhibitor degradation model is preliminarily built, which is expressed by desorption rate *k* of the inhibitor in Arrhenius Equation as:

$$k = A(s, t, i_n)\, exp\left(-\frac{E}{RT}\right) \tag{8}$$

Where *A* is the prefactor of desorption that is deemed to related to *s* (WSS), *t* (time) and i_n (the *n*-th testing inhibitor); *E* denotes the reaction energy of desorption; *R* is the Molar gas constant; *T* denotes the temperature. To measure the desorption rate, the surface coverage rate θ of the inhibitor should be first recorded in the experiment as:

$$\theta = \frac{CR_0 - CR_i}{CR_0}, \frac{d\theta}{dt} = k \tag{9}$$

Where CR_i and CR_0 the corrosion rates with and without the inhibitor. With a series points of θ, the desorption rate is accessible as the derivative of θ with respect to time. In general, the parameters *E*, *R* and *T* are accessible. Then, through measuring multiple values of *k* under different WSS, time and types of inhibitors, the relationship between inhibitor degradation and the three variables are expected to clarify in future experiment.

3.2.2.2 Dimensionality reduction for solving PDE

In this study, a dimensionality reduction method is introduced into the prediction of flow filed. Although some parameters need to be changed to obtain training data in different situations, many elements in the same scenario are fixed, e.g., the relationship between partial derivatives characterized by the Navier Stokes (NS) equation. This provides the possibility to reduce the flow

field data into the latent space with much less values that could be realized by the autoencoder (AE). This model first encodes the image input from original space into latent space and then decodes them back into original space. If the reconstruction loss between input and output is minimized a satisfactory level, the latent values could approximately represent the original PDE problem, and network training can be achieved at latent space, thus largely improving computational efficiency. As the initial research in performing dimensionality reduction method to deal with temporal prediction, the flow field data produced only by the NS equation used.

As the fundamental study, the training data is derived from NS equation with given initial conditions. In this study, initial conditions are produced by Gaussian random field, which controls the derivative of data within certain range to make the distribution smooth. Firstly, the framework of autoencoder is trained to reconstruct the flow filed in the global space. Once the reconstruction loss is minimized, the latent variables in autoencoder are used to represent the global distribution. On this basis, the Fourier neural operator (FNO) is applied to build the mapping between latent initial conditions and their subsequent development. The prediction results at latent space are finally decoded back into global space to realize the more efficient temporal prediction. The rest of this section will first give an introduction for the completed work in the application of autoencoder, and further illustrates the details of temporal prediction at latent space.

Figure 2.13 shows the framework of the applied autoencoder that consists of the encoder (upper part) and the decoder (lower part). The encoder receives a one-channel image as input and gradually suppress it into a 20-length vector through several convolutional layers, a flattening layer and a fully connected layer. The encoder performs an approximately inverse process from the vector to the original image. During the training process, traditional autoencoders optimize model parameters by minimizing the difference between input and reconstruction images. Since the encoder must represent data in a low-dimension space (usually called latent space), it is forced to learn the representation that maximizes the preservation of input information, which can remove certain redundance from the data and achieve dimensionality reduction. As illustrated in Figure 2.13, the used dataset contains 5000 time series of flow field with each one having 50 temporal snapshots. The first 4000 samples are for training, while the remains for testing. Later prediction at latent space still conforms to this division of samples. In the training of the autoencoder, the temporal dimension is reshaped into the sample dimension to adapt to its size of input with single image.

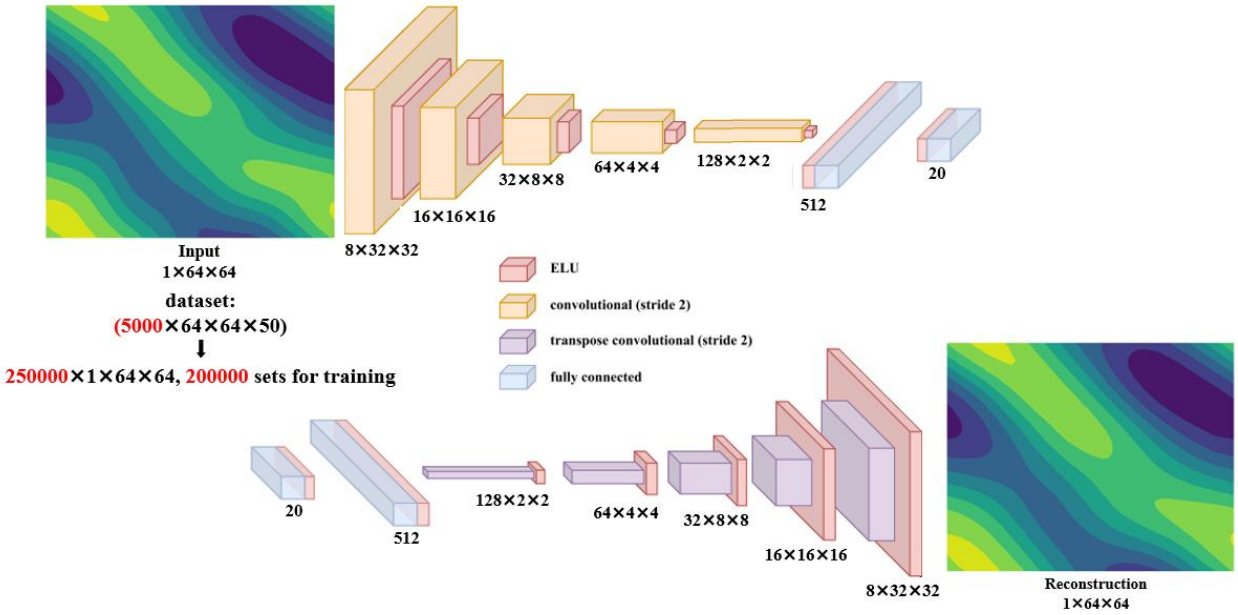

Figure 2.13. Schematic illustration of the applied autoencoder.

Except the reconstruction loss (RL), this study additionally introduces an item for the physics-informed loss (PIL) conforming the NS equation. The full loss function of the autoencoder is expressed as:

$$L = [RL] + [PIL] = \left[\frac{1}{N}\sum_{i=1}^{N}(x_i - \hat{x}_i)^2\right] + \left[\sum\left(w_t + uw_x + vw_y - \mu w_{xx} + \mu w_{yy} - f\right)\right] \quad (10)$$

Where N denotes the number of samples; x_i and $\hat{x}_i$ are input and reconstruction data, respectively; w_t, w_x, w_y, w_{xx}, w_{yy}, u and v are NS-related parameters that can be calculated from reconstruction data; μ and f are known viscosity and force.

With trained autoencoder, Figure 2.14 shows the comparison of several testing results. PIL aims to force data to conform to physical relationship and improve the generalization. From the figure we can see that the reconstruction loss of testing data has no significant change after adding physics information, although PIL is obviously decreased. However, generalization is mainly related to RL that characterizes the similarity between input and reconstruction image. For the training of the autoencoder, the improvement of models by physical information is limited.

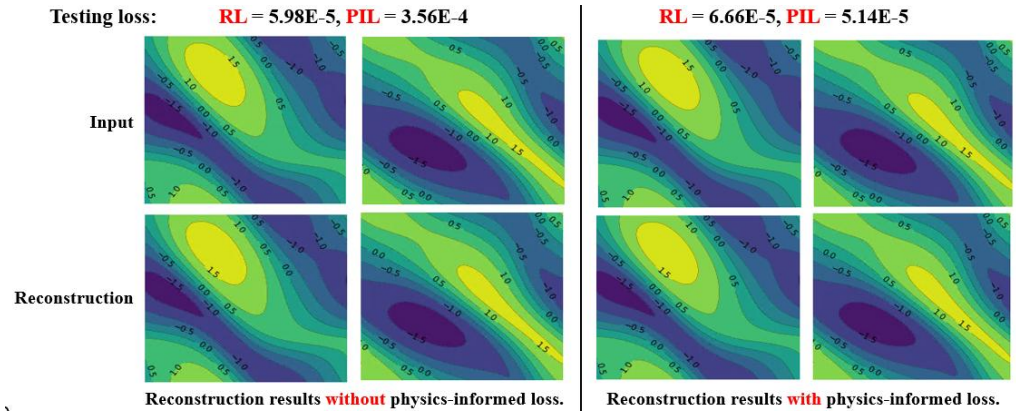

Figure 2.14. Comparison of reconstruction results with and without physics-informed loss.

The low RL indicates that the input can be well represented at latent space. Figure 2.15 shows the projection of the first two latent values after processed by principal component analysis in 10 samples, which indicates similar trajectories of various samples and the possibility to apply temporal prediction.

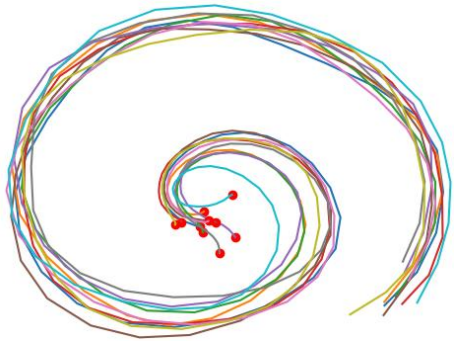

Figure 2.15. Projection of the first two latent values after processed by principal component analysis in 10 samples.

For the temporal prediction at latent space, the framework of FNO is still performed, which has been prove to effectively deal with temporal problems. Six prediction cases are set for comparison considering the prediction space, pattern and whether to use physics-informed loss, as listed in Table 2.1. Here, the prediction space distinguishes whether FNO is established at global or latent space. The patterns contain explicit and implicit prediction, both of which use the flow field at T_0 as input. The difference is that explicit cases predict solutions from T_1 to T_{25}, while implicit cases only have the T_{25} as the output. Besides, the applied PIL is similar as the loss function in training the autoencoder that constrains the output with the NS equation. For latent prediction, the output latent vectors would be decoded into global space to calculate PIL. It is noted that implicit cases only have one-time-snapshot output that the derivative w_t cannot be calculated. Thus, PIL is not applicable (NA) in implicit cases.

Table 2.1. Settings of different studied cases.

	Case 1	Case 2	Case 3	Case 4	Case 5	Case 6
Space	Original	Original	Original	Latent	Latent	Latent
Pattern	Explicit	Explicit	Implicit	Explicit	Explicit	Implicit
PIL	Yes	No	NA	Yes	No	NA

The testing results of original and latent prediction are shown in Figure 2.16 and Figure 2.17, respectively. Both the figures present the comparison between cases with and without PIL from T_1 to T_{25}. The loss at each time snapshot is characterized by mean (points) and standard deviation (error bars) calculated from 1000 testing samples. As the time snapshot far way from the initial condition, both the testing loss and uncertainty increase for the presented four cases. PIL help to reduce the testing loss in original predictions, but has almost no effect on latent predictions. Besides, original predictions have better performance reflected by testing loss than latent cases, which may because its complete spatial distribution could enhance the fitting of data relationships in the explicit temporal progression.

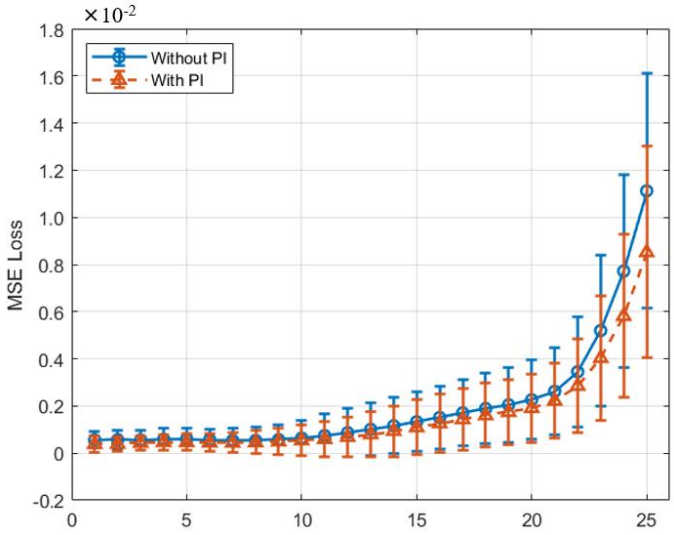

Figure 2.16. Explicit results of original prediction.

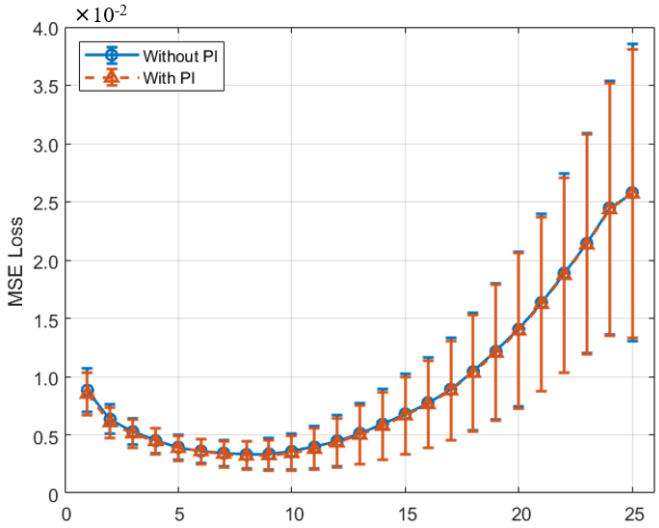

Figure 2.17. Explicit results of latent prediction.

The results for implicit cases are further shown in Figure 2.18 and Figure 2.19 with the form of possibility distribution. The loss of each sample is generally in a smaller level than explicit cases at T_{25}.

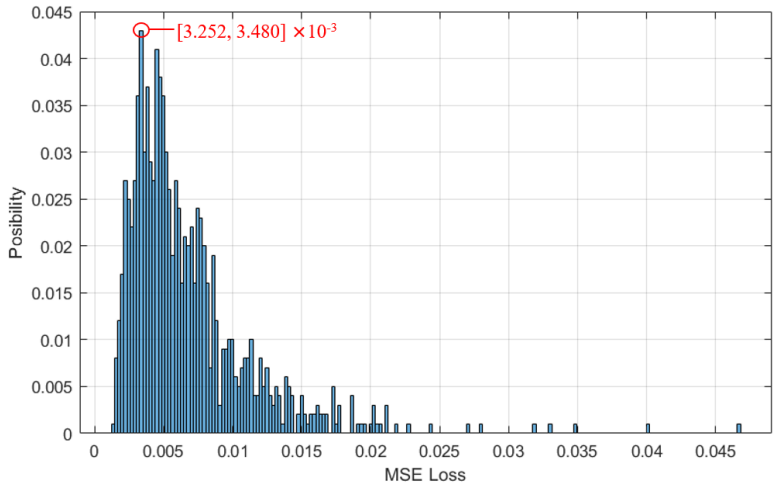

Figure 2.18. Implicit results of original prediction.

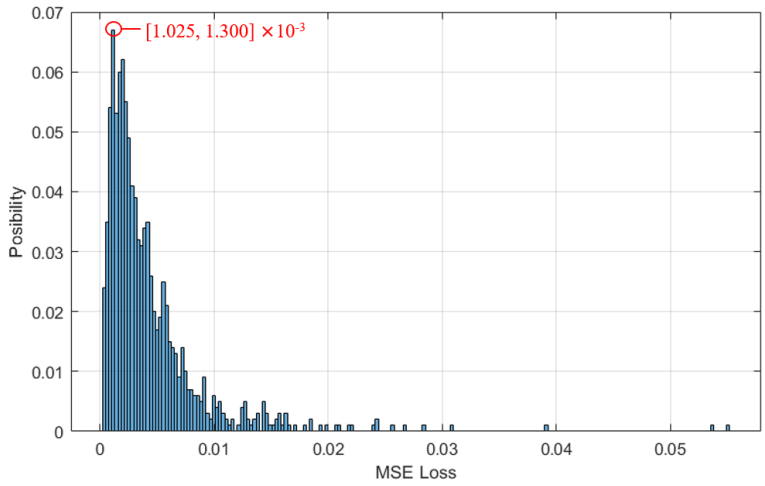

Figure 2.19. Implicit results of latent prediction.

Moreover, Table 2.2 gives the comparison of mean loss of 1000 samples and training time per epoch for each case. Here, the mean loss of explicit cases is only calculated from the data at T_{25}. It is obvious that original prediction achieves lower loss in explicit cases than implicit cases, i.e., 0.0085 versus 0.0257. Nevertheless, these two values could be still regarded in the same magnitude, while training at original space consumes much more time than latent space. For implicit cases, the latent result is surprisingly better than the original one. This is probably due to the elimination of certain redundance through dimensionality reduction and thus a more distinct matching between input and output. Similarly, the implicit training at latent space shows patent time efficiency compared with original prediction. Besides, it can recall that RL of the pre-trained autoencoder is in the magnitude of 10^{-5}, which is small enough for prediction loss that is larger than 10^{-3}. The comparison among the six cases could draw the conclusion that latent prediction can improve the learning for PDE-related problems without losing much accuracy and is therefore potential to be further applied to more complex fluent cases.

Table 2.2. Comparison of different cases at mean loss and training time per epoch.

	Case 1	Case 2	Case 3	Case 4	Case 5	Case 6
Space	Original	Original	Original	Latent	Latent	Latent
Pattern	Explicit	Explicit	Implicit	Explicit	Explicit	Implicit
PIL	Yes	No	NA	Yes	No	NA
Mean loss	0.0085	0.0111	0.0067	0.0257	0.0258	0.0043
Training time per epoch (s)	62.86	61.16	7.28	3.31	2.18	1.08

3.2.2.3 Multi-fidelity approach

Also, for high efficiency in data prediction, the multi-Fidelity approach is a powerful strategy used to enhance analysis and decision-making by integrating multiple data sets with varying levels of detail and accuracy. In obtaining precise fluent parameters, this approach has following key benefits:

- **Cost Optimization**: By using low-fidelity (LF) models for initial analyses and high-fidelity (HF) models for detailed validation, the overall cost of simulations is reduced. This balance allows for efficient allocation of resources.
- **Computational Efficiency**: LF models provide quick insights and preliminary results, reducing the need for extensive HF simulations in the early stages. This approach minimizes computational time and effort.
- **Enhanced Decision-Making**: The integration of both HF and LF data provides a comprehensive understanding of the system. LF models highlight general trends, while HF models confirm detailed interactions, leading to well-informed decisions.
- **Iterative Improvement**: Using LF models allows for rapid iterations and adjustments in the design process. HF models can then be applied selectively to verify critical aspects, ensuring a more robust and optimized design.
- **Risk Reduction**: By identifying potential issues early with LF models and validating solutions with HF models, the risk of errors and costly design flaws is significantly reduced.

Initially, we sought to use a 2-D coarse mesh as low-Fidelity and 2-D fine mesh as high-Fidelity, however we noticed that there wasn't enough difference in results to consider them to be of different fidelity. For instance, in this scenario, a U-bend pipe is taken into consideration for a simple 2-D single phase, second-order turbulent flow CFD simulation. The K-epsilon model is used with a medium coarse mesh and a fine mesh. The two results produced highly similar results with a similar computational time, as shown in Figure 2.20, which is not ideal enough to be considered as cases with different fidelity.

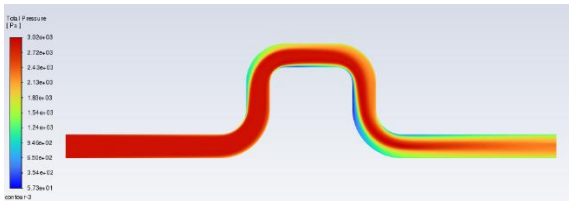

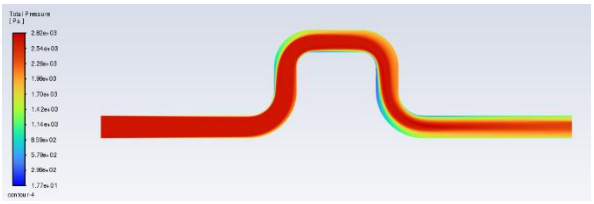

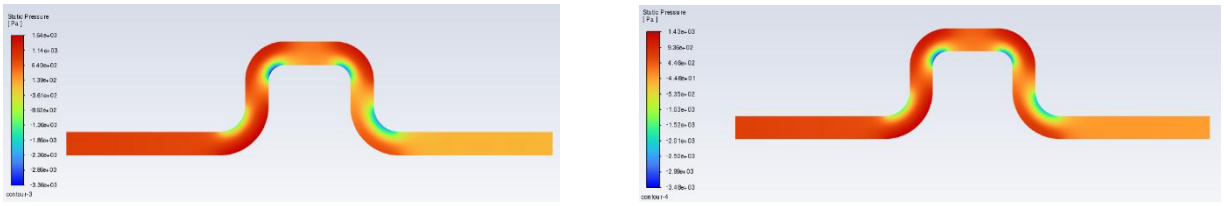

(a) LF case (b) HF case

Figure 2.20. Uncertainty quantification results with FNO.

Then, we switched things up to 2-D and 3-D, and corresponding CFD results of the computational maximum static pressures are listed in Table 2.3. It is noticed that we collect the sparse HF data, while LF data is relatively comprehensive, since our target is to predict ungiven HF information with the existing data. The obvious difference between LF results (2-D) and HF (3-D) results indicates the availability of using these cases for study.

Table 2.3. Comparison of maximum static pressure between fidelity

Velocity (m/s)	Maximum static pressure (Pa)	
	LF (2-D)	HF (3-D)
1	2601.12	
1.25	2549.56	
1.5	2890.36	
1.75	3270.16	
2	3669.73	4302.568
2.25	4158.18	
2.5	4728.33	5435.338
2.75	5323.68	
3	5994.28	6672.125
3.25	6715.60	
3.5	7599.13	8469.341
3.75	8346.92	
4	9158.34	10355.25
4.5	11050.02	
4.75	12052.50	
5	13136.21	

Using the data produced from CFD, the neural network for multi-fidelity prediction was established. Its architecture is as follow:

- **Input Layer**: Takes in multi-dimensional input that includes both LF and HF data points.
- **Convolutional Layer**: Extracts features from the input data using a convolutional neural network (CNN).
- **Dense Layers**: Comprises both a linear and non-linear path:
- **Linear Path**: Directly estimates the HF response.
- **Non-linear Path**: Captures the complex interactions between the LF and HF data.

- **Output Layer**: Combines the outputs of the linear and non-linear paths to predict the HF response.

The training of the neural network is accomplished in the Tensorflow module of Python, and Figure 2.21 shows the change of network loss over epochs. It can be seen that the training tends to converge after 100 epochs. As a result, Figure 2.22 depicts the curve for HF prediction (green line), which closely follows the trend of the high-fidelity actual values (red dots), indicating that the surrogate model effectively captures the detailed interactions and behaviors reflected in the HF data. The alignment of the model's predictions with the HF values demonstrates the success of integrating LF and HF data, leveraging the computational efficiency of LF data while maintaining the accuracy of HF data.

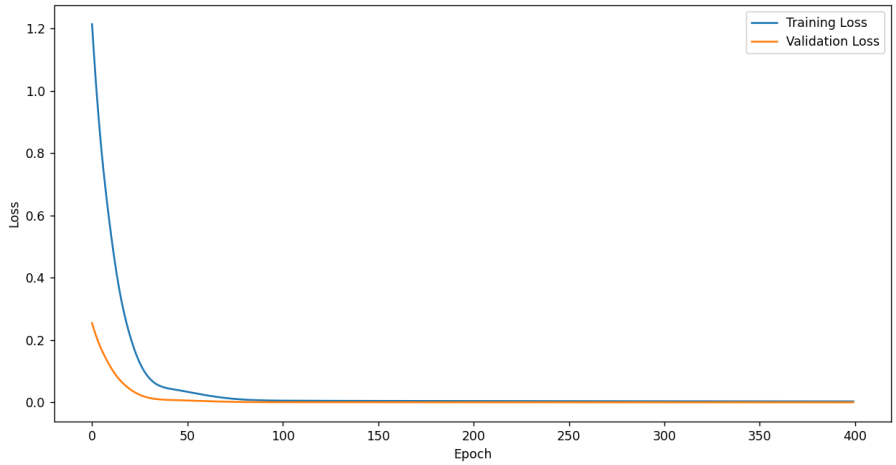

Figure 2.21. Loss over epochs in the training process.

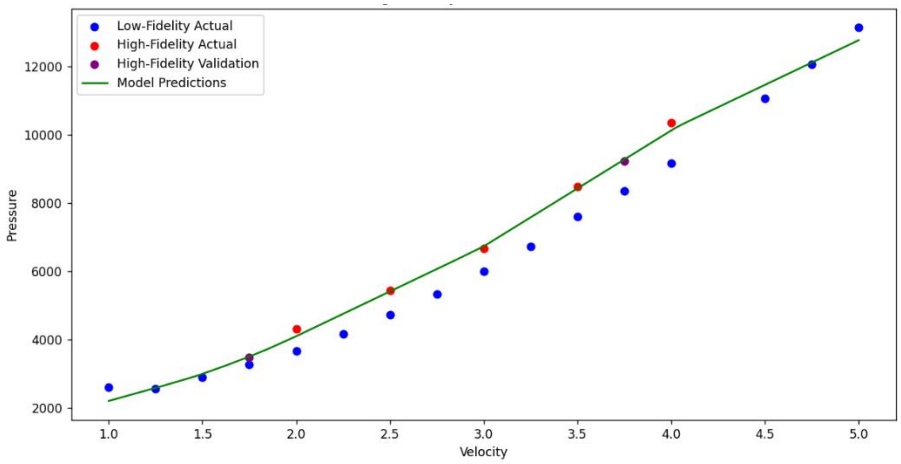

Figure 2.22. Prediction results of high-fidelity data.

On the basis of the above studies, a Bayesian optimization method with adaptive sampling is proposed, in which the Bayesian CNN computes the epistemic uncertainty for each prediction and is then used to determine the areas where additional HF data is required. The adaptive process operates as follows:

1. Initially, the network is trained using both LF and HF data.
2. During each iteration, the Monte Carlo Dropout technique is applied to compute the uncertainty at each prediction point by generating multiple predictions with dropout active. The epistemic uncertainty is derived from the variance across these predictions.
3. New HF data points are sampled at locations where uncertainty is highest, refining the model's predictive ability at minimal computational cost.

The results are shown in Figure 2.23 and Figure 2.24. The adaptive sampling approach iteratively selects the most informative data points, refining predictions only where needed. This method significantly reduced the Mean Squared Error (MSE) from 0.1431 in the original model to 0.1036 and improved the Root Mean Squared Error (RMSE) from 0.3783 to 0.2769 in a 10-dimensional model. The adaptive CNN also improved training efficiency, with final validation loss dropping from 1.8649 to 0.8649, demonstrating that fewer epochs were required to converge on an accurate solution. Training time increased only marginally (656.96 seconds to 734.72 seconds), but the gains in accuracy far outweighed this minor increase in computational cost.

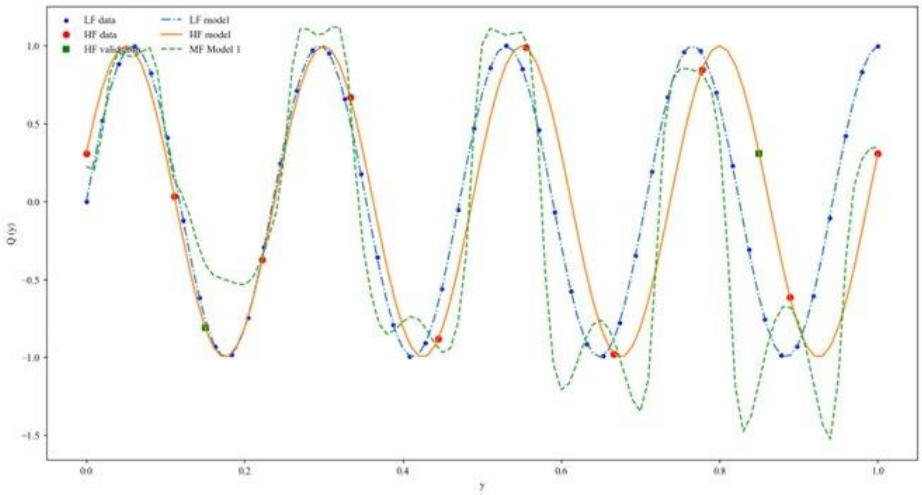

Figure 2.23. Results of the original case.

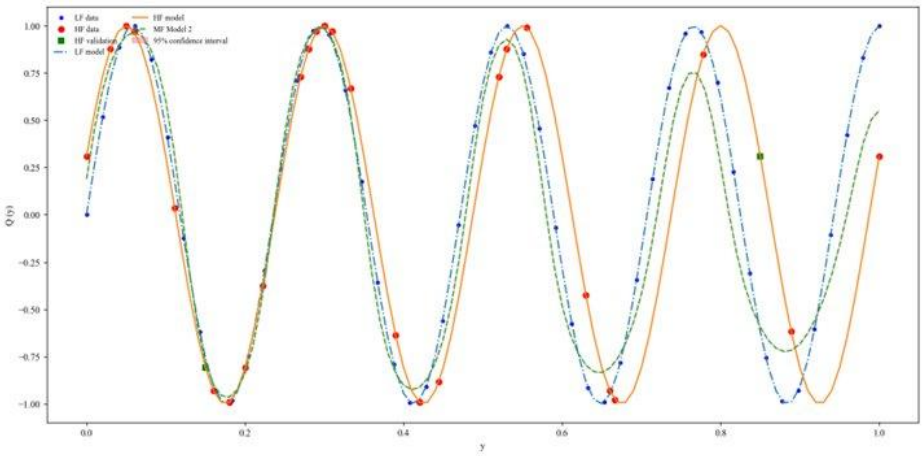

Figure 2.24. Result of the adaptive sampling case.

The Bayesian optimization method with adaptive sampling was further applied to a bending pipe case for validation. Here, the LF data was generated from the simplified 2D simulation of gas flow in a bending pipe, as shown in Figure 2.25. The more detailed HF data came from a 3D case model simulating turbulent flow in the same environment. These simulations modeled the flow condition of methane gas and mixture gas containing methane and inhibitor particles in a bent pipe under varying pressures. The mixture density and viscosity [3] are determined by the following equations:

$$\rho_{mix} = \alpha_{gas}\rho_{gas} + \alpha_{solid}\rho_{solid} \quad (12)$$

$$v_{mix} = v_{gas}(1 + 2.5\alpha_{solid} + 6.2\alpha_{solid}^2) \quad (13)$$

Where α and ρ denote the volume fraction and density, respectively. In this case, α_{gas} and α_{solid} are set as 0.9 and.0.1. Currently, the density of inhibitor particles is set as 1.5g/m^3 for simulation. More accurate values will be used when a specific type of inhibitor from Task 1 is applied. The Convolutional Neural Network (CNN) was trained on this multi-dimensional data, incorporating LF data and selectively adding HF data as needed.

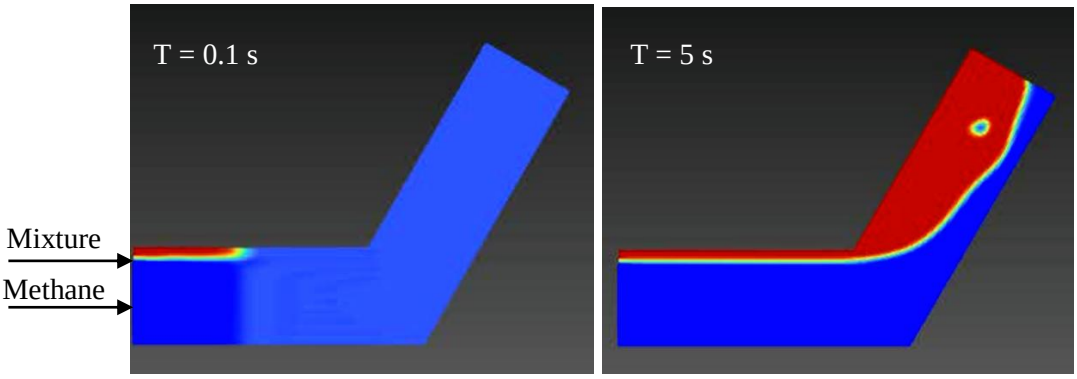

Figure 2.25: CFD case of the bending pipe.

The prediction result is shown in Figure 2.26, where the prediction green dashed curve satisfactorily fits the HF interpolation function. By applying adaptive sampling, the Bayesian CNN effectively interpolated between LF and HF results, particularly in turbulent flow scenarios where nonlinear behavior was prominent. Metrics such as Mean Squared Error (MSE) and Root Mean Squared Error (RMSE) were used to assess model performance. The adaptive CNN achieved a final MSE of 0.0831 compared to 0.1128 in the original model and RMSE of 0.1370, showing significant improvements through adaptive sampling.

The Bayesian optimization framework allowed the model to intelligently incorporate HF data only when it was crucial for accurate predictions. As a result, the multi-fidelity model closely followed HF predictions using far fewer HF data points, validating the method's effectiveness in real-world applications. This approach represents a major step forward in multi-fidelity modeling for gas pipeline simulations, where maintaining a balance between accuracy and computational cost is critical. The integration of adaptive sampling and Bayesian optimization ensures that resources are used efficiently, focusing on refining predictions in areas of high uncertainty while leveraging low-cost LF data where possible.

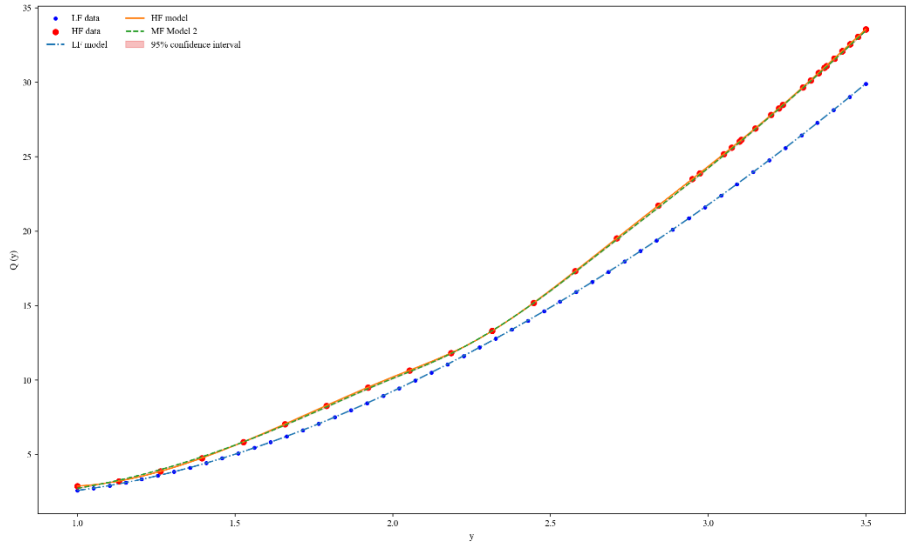

Figure 2.26. CFD case of the bending pipe.

4. Future Work for the next quarter (Q5)

Task 1: Design and Synthesis of Multi-compound Green Inhibitors

1) Based on the preliminary screening results in year 1, continue the testing for green inhibitors for gas pipeline protection.
2) Extend the literature research and experimental testing to identify environmentally friendly (green) corrosion inhibitors that might work best for gas pipeline applications.
3) Study the adsorption mechanisms and adjust green inhibitors' properties (functional groups) to enhance their interactions with the metal surface.
4) Select promising inhibitors based on their chemical properties, environmental impact, and corrosion inhibition effectiveness.

Task 2: Simulation-based inhibitor optimization in Gas Gathering and Transportation Pipelines

1) Perform latent prediction on inhibitor transportation with multi-channel data.
2) Integrate with experimental setup for demonstration.
3) combine the macro prediction of PDE solution and the micro prediction of wall sheer stress.

References

[1]. Guo, P., La Plante, E.C., Wang, B., Chen, X., Balonis, M., Bauchy, M. and Sant, G., 2018. Direct observation of pitting corrosion evolutions on carbon steel surfaces at the nano-to-micro-scales. Scientific reports, 8(1), p.7990. https://doi.org/10.1038/s41598-018-26340-5.

[2]. Cheng, Y.F., Wilmott, M. and Luo, J.L., 1999. The role of chloride ions in pitting of carbon steel studied by the statistical analysis of electrochemical noise. Applied Surface Science, 152(3-4), pp.161-168. https://doi.org/10.1016/S0169-4332(99)00328-1

[3]. Batchelor, G.K., 1977. The effect of Brownian motion on the bulk stress in a suspension of spherical particles. Journal of fluid mechanics, 83(1), pp.97-117. https://doi.org/10.1017/S0022112077001062